JOURNAL OF GEOPHYSICAL RESEARCH, VOL. ???, XXXX, DOI:10.1002/,

Post-emplacement cooling and contraction of lava flows: InSAR observations and a thermal model for lava fields at Hekla volcano, Iceland

Werner Wittmann[1], Freysteinn Sigmundsson[1]

Stéphanie Dumont[1], Yan Lavallée[2],

Corresponding author: W. Wittmann, Institute of Earth Sciences, University of Iceland, Sturlugata 7, Reykjavík IS-101, Iceland. (wew1@hi.is)

[1]Nordic Volcanological Center, Institute of Earth Sciences, University of Iceland, Reykjavík, IS-101 Iceland

[2]Department of Earth, Ocean and Ecological Sciences, University of Liverpool, Liverpool L69 3GP, UK

Abstract. Lava flows contract as they cool, causing progressive subsidence of the flow surface. Here we study this process by measuring and modelling the deformation of emplaced lava flows and the surrounding substrate. The temporal trend of vertical lava movements was investigated using interferometric analysis of synthetic aperture radar (InSAR) images from the 1991 and 2000 Hekla eruptions, covering periods of 23 and 12 years, respectively. Data from six tracks from three satellites, including both ascending and descending passes, were used to create 99 interferograms, from which trends of accumulated subsidence and subsidence velocities were derived. Subsidence rates are similar for both lava flows and decay approximately exponentially from about 20 mm/year five years after emplacement to about 2 mm/year 15 years after emplacement. A one-dimensional, semi-analytical model was fitted to the observed subsidence rates, with subsidence due to phase change calculated analytically, and subsidence due to thermal contraction calculated numerically using dilatometic constraints obtained experimentally. The initial thicknesses of the 1991 and 2000 lava fields, D_{1991} and D_{2000}, scaled thermal expansivity, $\gamma\alpha$, and thermal diffusivity, κ, are the crucial parameters influencing lava subsidence and subsidence rate. Inversion for these parameters reveal linear correlations between them. Best fitting results of inversions for D_{1991} range from 10 m to 27 m, for D_{2000} from 10 m to 30 m, $\gamma\alpha = (9 - 24) \times 10^{-6}$ K^{-1}, and $\kappa = (1 - 7) \times 10^{-7}$ m^{2}s^{-1}.

1. Introduction

Lava flows often form ideal surfaces for interferometric analyses of satellite-acquired synthetic aperture radar images (InSAR measurements), given their high backscatter due to their roughness and their high coherence due to their stable surface and lack of vegetation. Post-emplacement lava subsidence has been observed at many volcanoes, e.g. at Etna volcano in Italy [*Briole et al.*, 1997; *Stevens et al.*, 2001a], Okmok volcano in Alaska [*Patrick et al.*, 2004; *Lu et al.*, 2005, 2010], Kilauea volcano in Hawaii [*Peck*, 1978; *Hardee*, 1980; *Dietterich et al.*, 2012], Santiaguito volcano, Guatemala [*Ebmeier et al.*, 2012], Parícutin volcano, Mexico [*Chaussard*, 2016], and in Iceland e.g. at Krafla volcano in North Iceland [*Sigmundsson et al.*, 1997] and Hekla volcano in South Iceland [*Ofeigsson et al.*, 2011]. In Iceland, however, the underlying processes have not been studied in detail. Hekla volcano, which has erupted five times in the last half century, has been targeted by frequent satellite acquisitions over the last few decades, providing excellent opportunities to study the processes governing lava compaction, as InSAR interferograms can map lava deformation over a wide area with a high spatial resolution. This study addresses cooling, thermal contraction and the associated vertical movement of two lava flows at Hekla volcano over 23 years with detailed observations and modelling. When interpreting ground deformation at active volcanoes, it is essential to separate the different sources contributing to it, including the thermal contraction of recent lava flows. Petrological, physical [e.g. *Kattenhorn and Schaefer*, 2008; *Keszthelyi*, 1994], and rheological response of cooling lava flows may bias the retrieval of parameters associated with deeper magmatic processes, such as inferred magma source location and strength. Constraints on the thermal contraction of lava flows may thus enhance the resolution with which deep processes can be retrieved from ground deformation studies, furthering the aspiration of acquiring a rheological description of the state of magma during volcanic unrest.

InSAR techniques [*Rosen et al.*, 2000; *Massonnet and Feigl*, 1998] can map the change in distance along the line of sight (LOS) from ground to satellite between the acquisition times of SAR images by accurately comparing the phase of reflected radar waves in a set of SAR images. The accuracy of inferred LOS change can be as good as a few millimeters for patches of ground approximately 100 m^2 in size (e.g. *Massonnet and Feigl* [1998]; *Hooper et al.* [2012]), and thus it is a very useful technique to study post-emplacement deformation of lava fields. Georeferenced data of lava flow outlines allow detailed correlation of subsiding areas with the extent of lava flows. During the first phase of lava contraction, decorrelation in interferograms may occur because of the repacking of surficial clasts *Stevens et al.* [2001b], deformation of the viscous molten core of a lava flow [*Harris and Rowland*, 2001] and creeping of the underlying substrate [*Stevens et al.*, 2001a, b]. A pioneering study of lava cooling, solidification and accompanying degassing and its effect on vertical movements was undertaken between 1963 and 1967 at Alae lava Lake, Hawaii [*Peck*, 1978]. There, temperature and surface deformation measurements were carried out until the maximum temperature in the lava lake fell below 100°C, which was reached about four years after its emplacement. A recent study of the effects of solidification and degassing on vertical lava movement at Okmok volcano, Alaska, suggests that exsolution of gases may be an important contribution to volume changes during solidification near solidus conditions [*Caricchi et al.*, 2014].

Hekla volcano is located in south Iceland (Figure 1) at the junction of the Eastern Volcanic Zone (EVZ) and the South Iceland Seismic Zone (SISZ) (*Einarsson et al.* [1981], *Sigmundsson et al.* [1995]). The volcanic edifice is a southwest-northeast striking volcanic ridge, which rises 1488 meters above sea level. It is one of the most active volcanoes in Iceland [*Thorarinsson*, 1950], with recent eruptions in 1970, 1980/1981, 1991 and 2000. These eruptions began with an explosive phase (e.g. *Gudmundsson et al.* [1992]; *Gronvold et al.* [1983]; *Höskuldsson et al.* [2007]), before transitioning into the effusion of lava flows, which were emplaced onto the surroundings of the main volcanic edifice (Figure 1b). Two of the most recent lava fields are studied here: one formed during the 17 January - 11 March 1991 eruption, and the other during the 26 February - 8 March 2000 eruption. Both lavas were emplaced as 'a'ā flows and have similar basalt andesite chemical compositions [*Moune et al.*, 2006].

The lava deformation at Hekla is superimposed on a much wider deformation field at the volcano. Prior to, and after the eruption in 2000, a circular area of about 9 km radius around the main edifice of the volcano showed steady uplift at rates of up to 5 mm/yr [*Ofeigsson et al.*, 2011]. This is attributed to pressurisation of a source at a depth of $17-24$ km [*Ofeigsson et al.*, 2011; *Geirsson et al.*, 2012]. Co-eruptive deflation in 2000 was of a similar magnitude as the precursory inflation between 1993 and 2000 [*Ofeigsson et al.*, 2011]. Superimposed on the inter-eruptive uplift is a central region of subsidence, extending beyond the lava fields and exceeding the lava deformation signals. This latter observation may relate to viscous relaxation of the Earth due to loading of voluminous lava flows [*Grapenthin et al.*, 2010], or may be a consequence of the shape of the deep pressure source [*Geirsson et al.*, 2012]. The resulting inter-eruptive deformation between

1991 and 2000 of Hekla volcano forms a doughnut-shaped pattern of uplift surrounding the main edifice [*Grapenthin et al.*, 2010; *Ofeigsson et al.*, 2011; *Grapenthin et al.*, 2010]. This wide-deformation signal is only visible in InSAR time series analysis when carried out over a wider region than we focus on in this study.

2. Data analysis

2.1. Interferometric analysis

Interferometric analysis was carried out on SAR images of Hekla volcano acquired since 1993 by the European Remote Sensing (ERS), Envisat and COSMO-SkyMed (CSK) satellites. Six tracks from these satellites enable us to investigate post-emplacement contraction of lava flows for the last 20 years. An overview of the data and results are given in Table 1 and Figure 1. Interferograms were formed using the Doris software [*Kampes and Usai*, 1999]. Each satellite image was processed at full resolution corresponding to pixel sizes of 3 m for CSK data, and 12.5 m for ERS and Envisat data. In our analysis we used an intermediate TanDEM-X digital elevation model (DEM) formed from TerraSAR-X and TanDEM-X (TDX) satellite SAR images acquired in 2011-2012, with a resolution of 25 m $\times$ 12 m. Time series analysis was carried out on the resulting interferograms using the StaMPS software [*Hooper*, 2008; *Hooper et al.*, 2012], which implements an InSAR persistent scatterer (PS) approach [*Hooper et al.*, 2004]. In this approach, pixels are selected that have a single bright scatterer that reflects the radar signal transmitted by the satellite. No filtering is applied prior to the time series analysis. For each selected point, the StaMPS approach evaluates LOS change due to deformation and atmospheric error. DEM errors are estimated and removed. The PS approach works well on terrain such as the ‘a‘a lava fields at Hekla volcano because their textural variations and coarseness form persistent scatters at the satellite wavelength. A visual inspection of the interferograms was performed to exclude those with poor signal-to-noise ratio due to high atmospheric disturbance and little coherence over the lava flows, resulting from snow and large satellite baselines. Moreover, for the CSK time-series, no clear correlation between the phase and topography were observed and no correction for atmospheric signal was performed. For COSMO-SkyMed data the PS approach was considered because of the good signal-to-noise ratio obtained on the lava field. For the ERS and Envisat data set few PS pixels were selected by StaMPS, probably due to high satellite baselines, so a combined PS and Small Baseline (SB) approach was used. In the SB approach, interferograms are selected such their time interval is short and with a small difference in the satellite view, in order to minimize decorrelation in interferograms. The combined PS and SB approach combines advantages of both the approaches and can select more pixels than either of the approaches alone, when the InSAR data contains pixels with a range of scattering characteristics [*Hooper et al.*, 2012]. Phase unwrapping (inferring the appropriate number of whole wavelengths to add to the observed modulo 2π phase) is carried as part of the time series analysis. For one of the satellite tracks (CSK Track 2574) pre-unwrapping phase filtering was applied to suppress unwrapping errors, but for other data good results were achieved without this pre-filtering. The inferred average LOS changes for the different time intervals are based on INSAR time series analysis shown in Appendix 1. Figure 2 shows average LOS changes at Hekla volcano for the tracks listed in Table 1 and shown in Appendix 1. Each velocity image was referenced to its mean velocity in such a manner that the average velocity is subtracted and the sum of the LOS change of all pixels is zero. Each velocity map thus shows relative LOS changes. The central part of the volcano shows

LOS lengthening, partly overlapping with recent lava flows. Velocity maps overlapping in time and space from different satellite view angles allow an independent check of their noise level. Velocity maps of e.g. ERS Track 52 and ERS Track 324 for similar time spans (May 1995 - Jun 2000) were compared. Since both tracks are descending and have similar LOS unit vectors (compare Table 1), they should basically show similar results. The difference of the velocity maps shown in Figure 2a and b has a standard deviation of 4 mm/yr for the whole area, much smaller than the signal studied. Averaging pixels over limited areas should result in significantly reduced uncertainty.

The 1991 and 2000 eruptions primarily generated lava flows on the southern and south-western flanks of Hekla volcano (Figure 1). Since their respective emplacement, the lava tongues formed in 1991 and in 2000 show continuous subsidence during the period of this study (Figure 2 and figures in Appendix 1 showing time series of LOS change). They were selected as structures of interest for the present study aiming to constrain cooling-induced phase change and contraction.

LOS changes give the projection of a three dimensional displacement vector onto the direction of line of LOS from ground to satellite. Since SAR satellites are side-looking, the line of sight forms an "incidence angle", θ, with the normal of the surface of the Earth. The incidence angles for the different satellite configurations considered here are listed in Table 1 as well as the direction of the unit vector from ground to satellite. In the absence of any horizontal movements, the relation of LOS change to vertical movement can be reduced to:

$$d = \frac{\overline{\mathrm{LOS}}}{\cos\theta} \tag{1}$$

where d is the vertical movement and $\overline{\mathrm{LOS}}$ is the length of the displacement vector along the line of sight. In general there is, however, horizontal movement whose influence on the LOS change depends on the view angle. When ascending and descending tracks are available for the same region of interest and a similar time span, a linear combination of the LOS changes can be applied to approximate vertical and east displacement components. Adding together LOS changes from ascending and descending tracks results in a linear combination that is mostly dependent on the vertical displacement (see LOS unit vectors in Table 1), and subtracting them results in a linear combination mostly dependent on the east displacement component. These linear combinations can be scaled to reveal near-vertical and near-east displacement components [e.g. *Keiding et al.*, 2010]. In our case (Figure 3), this decomposition of coupled LOS changes shows the lava tongues selected as special target areas have a relatively well defined vertical displacement field. For 1993-1999, the near-east displacement components next to the 1991 lava tongue are similar compared to areas in its vicinity. For the 2000 lava tongue, an insignificant east displacement extends beyond the lava outlines during the period 2011-2014.

In order to investigate the correlation between areas of LOS lengthening and lava field extents, profiles striking West-East through both lava tongues were extracted (Figure 4). For both profiles, LOS rates change abruptly from near constant values on either side of the lava fields to higher negative values in the lava fields themselves, strengthening our assumption LOS changes over the flows are a function of internal processes within them. However, data to the West of both lava fields show a slight gradual change when approaching the lava edge, which can be interpreted as minor deformation of the surrounding host rock.

2.2. Temporal evolution of lava compaction

The subsidence time series was derived by selecting two sample areas well within each of the lava tongues in order to avoid edge effects (Figure 1). These sample areas within the lava tongues have well defined vertical displacements, and an east displacement that does not correlate with the lava extent (Figure 3). Relative LOS change between the sample areas and reference points outside the lava tongue is thus mostly due vertical displacement. Furthermore, based on pre-emplacement DEMs, we infer the lava tongues were emplaced on relatively flat ground and thus InSAR errors relating to significant topographic relief will be minimal. For both lava tongues, the average LOS changes of all pixels within circles of 100 m radius (centred at the orange and green stars in Figure 1) were extracted from the InSAR time series (see Appendix 1). In order to infer the internal deformation of the lava tongues, we subtracted the contribution from large scale deformation near the lava tongues, but outside them, represented by mean values from orange and green circles in Figure 1b., also of 100 m radius. In the case of the ERS and Envisat data, the averaging over one circle included typically about 48 pixels. For COSMO-SkyMed the number of points was about 1000 when no phase filtering was applied prior to unwrapping (CSK Track 2575), but reduced to about 12 for the case when filtering was applied prior to unwrapping (CSK Track 2574). However, in that case the scatter between pixel values was less. Taking the difference between the average value on a lava tongue and the corresponding average value outside of it reveals the lava-related LOS change. Uncertainty on the lava-related LOS change inferred in this way was based on the standard deviation of the selected pixels within the 100 m radius areas used. The uncertainty (see error bars on Fig. 5) is comparable for the different satellites used, although somewhat better for the CSK data.

Vertical deformation in the sample areas relative to their reference points was inferred using Equation 1, assuming no horizontal deformation due to internal processes within the lava tongues during the period of observation, in broad agreement with the inferred near-vertical and near-east components of displacements (when LOS change over lava is referenced to areas outside the lava). The LOS velocity field is thus scaled by $(\cos\theta)^{-1}$ to infer the vertical deformation. Figures 5a and 5b show the results for the lava fields of 1991 and 2000, referencing each time series to its first acquisition. As can be seen from Figures 5b and 2a-c, the region of the 2000 lava tongue shows slight subsidence before 2000, likely due to compaction of the 1980-81 lava field underneath. This trend was assumed to continue linearly after the eruption in 2000 and was subtracted from the data. Considering the processes causing deformation of the lava fields are continuous, the relative deformation data are transferred into deformation rates. This can be inferred from linear regressions between groups of data points within each time series, with the change between groups of points revealing deformation rates. Images from each summer period were typically considered as one group. Years with less than two data points were grouped together with a neighboring year. An example for ERS Track 52 is shown in Figure 5c. Data and errors from linear regression for the six InSAR tracks are shown in Figures 6a and 6b.

Clear evidence is found for decay of lava subsidence rate, ω, with time, t, since lava emplacement. The observed variation in subsidence was initially fitted with an exponential decay model:

$$\omega = \frac{\mathrm{d}\delta y}{\mathrm{d}t} = A \cdot e^{-t/b} \tag{2}$$

where δy is the vertical displacement, A is a constant and b is the exponential decay rate. For the lava tongue of 1991, the initial four years of data after emplacement were neglected since they show a different behavior. The best fitting parameters are $b = 4.7$ yrs^{-1} and $A = 51.5$. For the lava tongue of 2000, best fitting parameters are $b = 6.0$ yrs^{-1} and $A = 44.2$. The corresponding results are presented in Figures 6a and 6b.

By integrating equation 2, the accumulated deformation can be expressed as:

$$d = \delta y_0 + \delta y_{ts} - A \cdot b \cdot e^{-t/b} \tag{3}$$

$\delta y_{ts} + \delta y_0$ is the constant of integration and is different for each InSAR time series. It is split into two parts: δy_{ts}, which refers to the relative shifts of the single InSAR time series, and δy_0, which is the same for all InSAR time series and refers to the accumulated deformation before the first observation. The value for δy_0 cannot be resolved from our observations and is set to zero in Figures 6c and 6d, which show the best fits of Equation 3.

The lava subsidence rate follows approximately an exponential decay pattern for both lava fields. For the 1991 lava tongue, data before 1995 do not follow this exponential trend. Instead, the observations suggest lower subsidence rates during the first three to four years after the eruption. This is unlikely to result from InSAR related errors, such as atmospheric contributions, DEM errors or baselines, since six data points from two different satellite tracks show this behavior. This suggests that the lower initial subsidence rates are real and result from other contributing factors not considered here. A partial explanation may be degassing-induced expansion while the lava fields still have a molten core [e.g. *Caricchi et al.*, 2014], although it is uncertain how important this process is in our case. The exponential model presented above is simple, fits well with the data, and is therefore good to describe the temporal evolution. However, it does not explain the physics of the process involved, limiting the interpretation of the meaning of the A and b constants. A physics based model, considering the thermal evolution of the lava field as presented below, can on the other hand provide insights into the physical process taking place.

3. Thermal model

We used a thermal model to place constraints on the physical processes resulting from thermal contraction following the emplacement of lava. This one-dimensional model of lava cooling and contraction processes is subdivided into phases preceding and following complete solidification. Before solidification, latent heat of crystallisation is released between liquidus and solidus temperature conditions, and dissipated by conduction into the air and bedrock. After solidification the evolution of the lava flow is governed by conductive cooling. The problem then reduces to solving the heat diffusion equation and superimposed thermal contraction. The temperature distribution at the time when the lava fully solidifies is a parameter that needs quantification. During the initial phase of solidification, the thermal distribution within a lava flow and the substrate can be calculated with formulas derived from *Carslaw and Jaeger* [1959, Chapter XI, §11.2] and *Crank* [1984, Chapter 3.2]. Details of the method are presented in Appendix A, considering density changes and assumed constant initial temperature of the substrate. The predictions for lava contraction of this conduction based thermal model are shown in Figures 6a and

6b. Deviation from the smooth decline in subsidence rates (peak lowering of subsidence rates) near the beginning of the time series is associated with period when lava becomes fully solidified. At this time the internal temperature profile within the lava readjusts and for a limited time period less heat leaves the lava field, and subsidence rates are temporarily lowered. The main features of the modeling approach are summarized in the following paragraphs, but a full treatment and derivation of the governing equations is found in Appendix B.

A lava flow of initial thickness, D, and of initial homogeneous crystallization temperature, T_l, is emplaced on a flat ground (Figure 7). Note that for simplicity, we assume that crystallization takes place at a given temperature instead of a temperature interval. The coordinate system is chosen with origin $y = 0$ at the bottom of the flow, and positive values upwards. The temperature of the air, T_a, and of the substrate, T_b, at a large depth, $y \rightarrow -\infty$, are kept constant throughout the simulation. The lava flow solidifies from above and below, and upper and lower crusts develop. Under these assumptions, calculations for the lower and upper boundary are independent of each other as long as a liquid core exists. During this solidification process, the subsidence rate, u, of the lava flow due to thermal contraction, u_{th}, and due to density changes at the upper (u_{up}) and lower (u_{low}) crusts is given by

$$u = u_{up} + u_{th} + u_{low} \tag{4}$$

Before full solidification, the temperature distribution is described by equations A25 - A28 in Appendix A. In order to estimate the contribution from thermal contraction, these equations are implemented in a finite difference scheme. After each time step, the thermal contraction is calculated. The thermal contraction of a lava flow is a volumetric process, and one has to consider how the linear coefficient of thermal expansion (α) relates to the change in elevation. Contraction of the horizontal dimensions may be translated into lowering of the lava flow surface, in addition to the thermal contraction in the vertical dimension. In order to account for that possibility, we calculate the contraction in vertical dimension according to:

$$\Delta h = \gamma \alpha h \Delta T \tag{5}$$

where h is height and Δh change in height. If the coefficient γ equals 1, the basic linear thermal expansion formula is retrieved. If all the volumetric contraction of a cube element goes into lowering its height, then γ would equal 3. Intermediate value may also apply; when studying lava flow contraction *Chaussard* [2016] used a value of $\gamma = (1+\nu)/(1-\nu)$, where ν is the Poisson's ratio. For the typical value of $\nu = 0.25$, then $\gamma = 1.7$.

After complete solidification, temperature changes within the size of the finite differences are calculated via the heat diffusion equation. Between each two adjacent time steps, the thermal contraction within the lava field is given by equation 5. On this basis, the subsidence as well as the subsidence rate are calculated. Our modeling approach is simpler than taken in some of previous studies [e.g. *Patrick et al.*, 2004] as it is partly based on analytical equations and their implementation in a finite difference scheme.

The model is incorporated into an inversion procedure in order to find the best fitting values for thermal expansivity, thermal diffusivity and the lava thicknesses for each of the two study areas. Best fitting results are shown in Figures 6a,b and 12.

Equations A25 and A26 are dependent on time. Applying thermal contraction according to Equation 5 varies the size of the finite differences after each time step and introduces a small error when the temperature distribution is again calculated from Equations A25 and A26. However, compared to neglecting thermal contraction, the resulting deviation from the analytically imposed temperature distribution is presumably small.

4. Inversion

The thermal model is an approximation of the cooling and solidification processes. It accounts for conduction and constant values of the parameters throughout the whole simulation period. The parameters influencing contraction and contraction rate are the initial lava thickness, thermal expansivity and thermal diffusivity. Densities of the liquid and solid phases, latent heat and specific heat affect the temperature distribution and contraction during solidification. Density values for the liquid and solid phases were calculated using the software MELTS [*Ghiorso et al.*, 2002], based on the chemical composition of the 1991 lava reported by *Gudmundsson et al.* [1992] and of the 2000 lava reported by *Moune et al.* [2006]. At the liquidus temperature, $T = 1176°\text{C}$, the density of the liquid phase at atmospheric pressure is 2.66×10^3 kgm^{-3}, while the density becomes 2.80×10^3 kgm^{-3} when fully solidified at $T = 975°\text{C}$.

Due to the partly analytical calculations of the model, a constant latent heat throughout the crystallization interval was used. Direct measurements of latent heat were carried out by *Lange et al.* [1994]. Their results show that latent heat varies from liquidus to solidus with a peak close to liquidus temperature. Constant values for latent heat of $L = 320 \times 10^3$ Jkg^{-1} and for specific heat of $c = 1200$ Jkg^{-1}K^{-1} were used [*Turcotte and Schubert*, 2002].

4.1. Inversion range of parameters in the thermal model

Inversions for best fitting models were carried out for four free model parameters: thermal expansivity, α, thermal diffusivity, κ and initial thicknesses for both lava fields, D_{1991} and D_{2000}. The two lavas show similar chemical compositions [*Moune et al.*, 2006], and it is therefore assumed that the thermal properties, α and κ, are the same for both lava tongues.

The initial thicknesses of the emplaced flows of 1991 and 2000 are constrained by values determined by comparison of differential digital elevation models (DEMs) by *Pedersen et al.* [2016]. For the lavas of 1991, a DEM from digital photogrammetry of aerial photographs taken in 1979 was subtracted from the iDEM specified in Section 2.1. The differential DEM for the 2000 lavas was created using an EMISAR DEM of 1998 [*Magnússon*, 2003] and the TanDEM-X iDEM. The 1998 DEM was created from SAR survey using EMISAR, an airplane borne dual frequency (L- and C-band) fully polarimetric SAR system developed in Denmark for remote sensing applications [*Christensen et al.*, 1998]. Lava thicknesses estimated in this way give a range of $15 - 19$ m for the 1991 tongue and a range of $12 - 14$ m for the 2000 lava tongue [*Pedersen et al.*, 2016].

A priori constraints for parameter ranges of linear thermal expansivity and diffusivity are based on laboratory measurements and literature values for basaltic andesite and basalt as presented in Table 2. We carried out linear dilatometric measurements in the laboratory at the University of Liverpool using a Hyperion thermo-mechanical analyser TMA402 F1 from Netzsch with a length resolution of 0.125 nm. Four samples from the 2000 Hekla lava tongue were selected to assess the range of thermal expansion coefficient for rocks with porosities ($10.5 - 22.4$ %) spanning the range dominant at this lava flow.

The dilatometric measurements were conducted on small (5 mm diameter by 6 mm high) cylindrical cores in argon atmosphere, at an applied axial stress of 3 N rate and at a heating rate of 2°C/min up to 1000°C; the sample was then cooled down at the same rate. Prior to each measurement, a baseline measurement was first conducted on an alumina ceramic standard (with identical geometry) to assess the thermal response of the sample assembly. Then, a sample was measured with the same load and heating conditions, and the linear thermal expansion of the sample was corrected to remove any thermal-expansion effects from the sample assembly. The data first highlight the minor artifact of thermal lag and equilibration at low temperatures up to 150°C (Figure 8). The data shows a near constant expansion coefficient (α) in the range 150°C $< T <$ 600 $-$ 700°C and suggest a value of $(8.4 \pm 0.6) \times 10^{-6}$K^{-1} (see Figure 8). Above this temperature, we note an increase in thermal expansivity due to phase change in the sample (likely due to the presence of plagioclase in the mineralogical assemblage of these rocks). The peak and subsequent decrease in expansion coefficient coincide with the onset of partial melting at ca. 980°C, which mechanically results in softening of the sample (hence the mild contraction due to relaxation of the applied stress). For the problem tackled here, the measured value for the linear expansion coefficient was considered in the inversion. A priori bounds on the γ coefficient in equation 5 were set to 0.5-3, accounting for the possibility that all volumetric contraction would result in height contraction, but also that the effective coefficient of linear expansion would be lower than the measured value.

4.2. Inversion results

In order to find the contraction rate derived from the thermal model that best fits the data presented in Figures 5 and 6, a non-linear inversion estimate of the free parameters was carried out. The inversion was carried out in the programming language Python. The Scientific Library for Python (SciPy) provides an implementation of inversion with a limited memory Broyden-Fletcher-Goldfarb-Shanno (BFGS) scheme using simple box constraints (L-BFGS-B) of the basin-hopping algorithm by *Byrd et al.* [1995]. It is based on Monte-Carlo methods and the Metropolis algorithm. By allowing parameters to jump within the parameter ranges with decreasing probability, the likelihood of finding the globally best fitting parameters is maximized. A few hundred inversions were run starting from randomly chosen sets of parameters within the *a priori* constrained intervals (Table 3). Initially, the inversion was carried out for latent heat L and specific heat c as well, but they showed little influence on the inversion and thereafter their values were fixed to 320×10^3 Jm^{-3}K^{-1} and 1200 Jkg^{-1} [*Turcotte and Schubert*, 2002], respectively, in order to speed up calculations.

Inversions for each lava tongue separately revealed little difference for values of α and κ. Since it is assumed that the two kinds of lava of 1991 and 2000 have similar thermal properties, a joint inversion for the 1991 and 2000 lava tongues was carried out. Figure 9 shows the results of the inversions, which all have similar root-mean-square errors (RMSE) of about 1.53 mm/yr. Free parameters are the thicknesses of both lava tongues, thermal diffusivity and the linear coefficient of thermal expansion, α, multiplied by the γ coefficient to consider volumetric contraction. We refer to $\gamma\alpha$ as the effective vertical thermal expansivity. The resolved values show strong correlation between pairs of parameters. For a specific value of α, a narrow range of the corresponding thicknesses for both lava tongues and the value for κ can be determined, and vice versa. Figure 9 further shows, that for any specific thermal diffusivity and effective vertical thermal expansivity, the 2000 lava tongue is similar in thickness as the 1991 lava tongue. This finding is only consistent with the different a priori ranges for the thicknesses of the lava tongues, if both of them are similar. Considering uncertainties, we therefore consider solutions with lava thickness in the range of $11 - 19$ m. We suggest the corresponding set of parameters is the preferred solution to the problem, fitting the thermal model and the a priori bounds on the lava thickness. This implies $\gamma\alpha$ has a value of $14-23 \times 10^{-6}\mathrm{K}^{-1}$ and considering the laboratory measured value of α, the γ coefficient has a value of $1.69-2.41$. Accordingly, the lowering of the lava surface is highly effective in accommodating the volumetric contraction of the lava tongues. The range for the thermal diffusivity is $1.07-3.00 \times 10^{-7}$ m^{2}s^{-1}. It is lower than found by Peck [1978] for the Alae lava lake, but near the lower end of diffusivity values found from thermal modeling of a lava field on Okmok volcano. In that case, the range to tabulated parameters [*Patrick et al.*, 2004, Table 3] gives diffusivity values in the range $3.5-8.6 \times 10^{-7}$ m^{2}s^{-1}. Considering our values for thermal diffusivity in the context of these other studies, we infer that the highest diffusivity value in our identified range is the most likely (Fig. 12). We conclude the studied lava tongues at Hekla are not good conductors of heat, and may have some internal insulation preventing heat to escape. We suggest cracks or high porosity layers, isolated from air temperature, at depth in the lava field hinder the flow of heat, and are the cause for the low effective heat diffusion. Our simple thermal model can thus explain the observed deformation upon two conditions: lowering of lava fields is effective in accommodating the full volumetric contraction of the lava, and heat remains for long in the lava fields because of relatively low effective heat diffusion.

5. Discussion

The deformation data presented here are based on InSAR observations. Application of the presented method is therefore not only limited to easily accessible effusive eruption sites, but also applies to remotely located volcanoes. Iceland in particular, with its overall sparse and slowly growing vegetation, offers excellent preconditions for InSAR observations. Based on highly coherent data sets from six satellite tracks spanning time periods of up to 23 years we find clear exponentially decaying rate of lava subsidence over long time, excluding the initial few years after emplacement. A model of the thermal evolution of a lava field and associated lava subsidence was implemented, considering both volume contraction due to phase change and cooling. The model predicts subsidence and decaying subsidence rates as observed, and allows for inversions for the best fitting values for lava thickness, effective vertical thermal expansivity and thermal diffusivity. The parameter values derived from the thermal model are "effective" and depend on the simplified model assumptions.

The model assumes a constant temperature of the flow substrate at the time of lava emplacement. This may be an issue for the 2000 lava flow as it was emplaced on top of the lava flow of 1980-81, which shows ongoing subsidence in Figures 2a-c and 5b. The data after the year 2000 were corrected for a linear trend that supposedly originates from the lava flows of 1980-81. But the thermal model does not take into account a temperature distribution originating from a still cooling and contracting lava of 1980-81. The influence of this simplification was tested by incorporating a substrate below the 2000 lava field with elevated temperatures due to the 1980-81 lava flow. We found it had a minor influence on predicted subsidence and since the real temperature of the substrate is unknown, we preferred the simple model of constant temperature for the flow substrate.

Inversions for thickness of both the lava tongues studied result in similar values (Figure 9). This is only in agreement with thickness measurements from differential DEMs of the lava tongues if they are of similar thickness, about 14-15 m. For these thickness values, a unique pair of effective thermal expansivity and thermal diffusivity was derived (see Figure 9). The derived values maybe influenced by the model simplifications, and effects such as viscous response of the Earth, clast repacking of underlying lava fields and creeping of the flow core were not taken into account. A viscous relaxation of the lava substrate has been invoked as an explanation for lava displacement, in particular when subsidence extends outside lava fields. For example, *Briole et al.* [1997] found evidence for such process at Etna volcano and a clear local deformation signal extending outside a newly emplaced lava flow. We find no similar significant signal at Hekla. At Hekla, a much wider viscoelastic relaxation signal due to lava loading has, however, been suggested by *Grapenthin et al.* [2010]. Their model considers lava load emplaced on a few km thick elastic uppermost crustal layer above a viscoelastic base. The predicted signal from this process, when combined with a pressure increase at depth, could potentially explain the volcano-wide deformation signal at Hekla (inflation signal with a central subsidence). For our detailed study of lava tongues, its effect would mostly cancel out when interpreting relative LOS changes with our approach over a limited area (the signal is about the same at the lava tongues and just outside them). Additional cooling due to rainfall, wind and radiation were also not incorporated specifically in our model. *Patrick et al.* [2004] found effects from radiation during an initial period of lava cooling (about 200 days), but having less significant effect afterwards. Even if rainfall affects cooling longer, an approach as taken by *Shaw et al.* [1977] and applied by *Patrick et al.* [2004] would as well mostly cool the lava in an initial period. The bulk material of the lava is dense, thus stopping the water to percolate much inside the bulk. Since we keep the surface of the lava at 0°C, part of the cooling effect of water is absorbed in this assumption. Furthermore, the initial period after emplacement, which is affected by both radiation and direct effects of rainfall, is not the main topic of our study due to timing of the InSAR acquisitions in our case. These effects should, however, be considered in further studies of other lava fields, with more dense InSAR coverage. These effects could increase cooling rates and there may also be mechanically influenced subsidence, so that thermal contraction only accounts for a fraction of the total subsidence. However, despite the simplicity of the model, the inversion parameters are in the right order of magnitude, and the derived values should be interpreted as effective values, with exact values influenced by the model assumptions.

Noting that *Peck* [1978] reports a maximum temperature of about 100°C after approximately four years after emplacement of the solidifying Alae lava lake with an average thickness of 14 m, it seems likely that lava may cool at very variable rate. This thickness is similar as our inferred thickness for the Hekla lava tongues studies, but our inferred maximum temperature in the flow core after four years is about 650°C. Based on this we suggest the effective thermal conductivity within lava fields in general is highly variable, and microcracks isolated from ambient air may act as insulators.

Investigation of contraction of lava flows, which are generally accessible for sampling, investigation, and importantly, visual inspection, is a step towards understanding of magma body definition and evolution at depth. Volume variations at depth - whether due to crystallisation, volatile exsolution, thermal contraction, etc. - may induce deformation on the surface of the Earth, offering opportunities for observations and in return for the generation of inverse models that may define the physical-chemical evolution of magmatic bodies. This study is therefore a step towards improving our understanding of magmatic systems necessary for improved monitoring strategies in volcanic environments.

6. Conclusion

The combination of InSAR data over lava flows spanning time periods up to 23 years after emplacement and an associated thermal model provide new insights and interpretations of cooling and contraction of lava flows. When line-of-sight (LOS) changes over lava fields are corrected for LOS changes at reference areas outside the lava fields, the temporal and spatial evolution of lava subsidence can be derived. At Hekla volcano, corresponding subsidence rates decay from about 20 mm/year after five years to about 2 mm/year after 15 years after emplacement, with an approximately exponential decay. A simple thermal model based on heat conduction can reproduce the observations. Despite the simplicity of the model, all inversion parameters are in the right order of magnitude. *A priori* information on lava thickness values allows us to select preferred values for effective vertical thermal expansivity and thermal diffusivity, based on inversion results. Volumetric effects of lava contraction due to cooling are absorbed into lowering of the lava fields, and we infer a low effective thermal diffusivity. We suggest remaining deviation of inversion parameters from *a priori* parameter ranges is due to additional cooling effects beyond conductive cooling. In general, a combined approach of InSAR observations and thermal modeling is well suited to study lava fields at volcanoes worldwide, including remote locations.

Appendix A: Derivation of the governing equations for a cooling lava field

The cooling and contraction process can be subdivided into cooling before and after full solidification. Before the lava is fully solidified, there is need to consider latent heat at the phase transition. This mathematized problem of the development of a crust due to solid-liquid phase transition is commonly known as Stefan problem. The following derivation of equations are a variation and adaptation of [*Carslaw and Jaeger*, 1959, chapter XI] and [*Crank*, 1984, chapter 3.2].

The scheme of the model is shown in Figure 10. The lava flow is emplaced at a homogeneous temperature before it starts cooling. The temperature of the uppermost layer (air) is kept constant at all times, thus releasing heat that is transferred by conduction to this element. Heat is also transferred to the flow substrate, which itself is kept at a constant temperature at all times at large depth. Each section of the model has its own thermal and mechanical properties. These are the density ρ, the specific heat c, the thermal conductivity k and the thermal diffusivity κ. As the lava flow cools, crusts evolve from the bottom and the top of the flow. Their moving and time dependent coordinates of the boundaries are $s_{low}(t)$ and $s_{up}(t)$.

Since the lava flow solidifies from the top and below, both upper and lower crust develop and each problem can initially be evaluated separately. The left-hand side of Figure 11 schematically refers to the lower part of the lava flow and shows a slab of bedrock, crust and liquid lava, with parameters of interest for each region.

Similarly, the right-hand side of Figure 11 shows the equivalent problem for the upper crust. In order to make use of similarities, the coordinate system in this case was mirrored. In both cases, a crust develops and moves in positive y-direction upwards with $s(t)$, which denotes the position of the surface of phase transition. Simplifying assumptions are a single temperature at which the lava solidifies, rather than a melting range between liquidus and solidus temperature. Furthermore, it is assumed that the lava is incompressible and that the crust has a higher density than liquid lava, i.e. $\rho_1 > \rho_2$.

The governing system of equations in this case becomes:

$$\frac{\partial T_0}{\partial t} = \kappa_0 \frac{\partial^2 T_0}{\partial y^2} \quad , \text{ for } y < 0 \tag{A1}$$

$$k_0 \frac{\partial T_0}{\partial y} - k_1 \frac{\partial T_1}{\partial y} = 0 \quad , \text{ for } y = 0 \tag{A2}$$

$$\frac{\partial T_1}{\partial t} = \kappa_1 \frac{\partial^2 T_1}{\partial y^2} \quad , \text{ for } 0 < y < s(t) \tag{A3}$$

$$k_1 \frac{\partial T_1}{\partial y} - k_2 \frac{\partial T_2}{\partial y} = L\rho \frac{\mathrm{d}s}{\mathrm{d}t} \quad , \text{ for } y = s(t) \tag{A4}$$

$$\frac{\partial T_2}{\partial t} = \kappa_2 \frac{\partial^2 T_2}{\partial y^2} + \frac{\rho_1 - \rho_2}{\rho_2} \frac{\mathrm{d}s}{\mathrm{d}t} \frac{\partial T_2}{\partial y} \quad , \text{ for } y > s(t) \tag{A5}$$

T_0, T_1 and T_2 refer to the temperatures of the bedrock, the crust and and the liquid region of lava. The set of equations requires some explanations:

1. Equation A1 and A3 are the heat diffusion equations for the bedrock and the solidified lava.

2. Equation A2 is the boundary condition between these two regions.

3. Equation A4 is the boundary condition between liquid and solid phase of the lava. When this boundary moves a distance ds, a quantity of heat $L\rho_2 \mathrm{d}s$ per unit area must be removed by conduction [*Carslaw and Jaeger*, 1959].

4. Equation A5 is the heat diffusion equation in the liquid lava with an additional term taking into account the densification during solidification, which causes motion of the liquid above the crust. During solidification, the relative volume change per unit area is $\frac{\rho_1 - \rho_2}{\rho_2} \mathrm{d}s$.

From the last point, a velocity u of the moving liquid can be deduced:

$$u = \left(1 - \frac{\rho_1}{\rho_2}\right) \frac{\mathrm{d}s}{\mathrm{d}t} \tag{A6}$$

This set of equations is valid for both the lower and the upper crust, but the initial and boundary conditions are different. For the lower crust, the heat transfer to the bedrock (initially homogeneously at temperature T_b) has to be taken into account, which is fulfilled by the following boundary conditions:

$$T_1 = T_0 \quad , \text{ for } y = 0,\ t \geq 0 \tag{A7}$$

$$T_2 \to T_l \quad , \text{ for } y \to \infty,\ t \geq 0 \tag{A8}$$

$$T_0 \to T_b \quad , \text{ for } y \to -\infty,\ t \geq 0 \tag{A9}$$

$$T_1 = T_2 = T_m \quad , \text{ for } y = s(t),\ t \geq 0 \tag{A10}$$

T_m is the temperature of the melting point and T_l the temperature of emplacement of the lava flow. A solution to Equation A1 is

$$T_0 = A + B \cdot \operatorname{erf} \frac{y}{2\sqrt{\kappa_0 t}} \tag{A11}$$

And for Equation A3:

$$T_1 = C + D \cdot \operatorname{erf} \frac{y}{2\sqrt{\kappa_1 t}} \tag{A12}$$

At the phase boundary $y = s(t)$, T_1 must be equal to the melting point T_m, and this must hold at all times t. From Equation A12 then follows that $s(t)$ must be proportional to $\sqrt{t}$:

$$s(t) = 2\lambda\sqrt{\kappa_1 t} \tag{A13}$$

λ is a dimensionless coordinate determined from Equation A4. A solution to Equation A5 is:

$$T_2 = T_l - D \cdot \operatorname{erfc}\left(\frac{y}{2\sqrt{\kappa_2 t}} + \lambda \frac{\rho_1 - \rho_2}{\rho_2}\sqrt{\frac{\kappa_1}{\kappa_2}}\right) \tag{A14}$$

Applying these boundary conditions to the lower crust and calculating the constants A, B, C, D reveals:

$$T_0(t) = T_b + \frac{k_1\sqrt{\kappa_0}T_m}{k_0\sqrt{\kappa_1}\operatorname{erf}(\lambda_{low}) + k_1\sqrt{\kappa_0}} \cdot \left(1 + \operatorname{erf}\frac{y}{2\sqrt{\kappa_0 t}}\right) \tag{A15}$$

$$T_1(t) = T_b + \frac{T_m - T_b}{k_1\sqrt{\kappa_0} + k_0\sqrt{\kappa_1}\operatorname{erf}(\lambda_{low})} \cdot \left(k_1\sqrt{\kappa_0} + k_0\sqrt{\kappa_1}\operatorname{erf}\frac{y}{2\sqrt{\kappa_1 t}}\right) \tag{A16}$$

$$T_2(t) = T_l - \frac{T_l - T_m}{\operatorname{erfc}\left(\lambda_{low}\sqrt{\frac{\kappa_1}{\kappa_2}\frac{\rho_1}{\rho_2}}\right)} \cdot \operatorname{erfc}\left(\frac{y}{2\sqrt{\kappa_2 t}} + \lambda_{low}\frac{\rho_1 - \rho_2}{\rho_2}\sqrt{\frac{\kappa_1}{\kappa_2}}\right) \tag{A17}$$

$$\frac{k_0\sqrt{\kappa_1}e^{-\lambda_{low}^2}}{k_1\sqrt{\kappa_0} + k_0\sqrt{\kappa_1}\operatorname{erf}(\lambda_{low})} - \frac{k_2\sqrt{\kappa_1}(T_l - T_m)e^{-\lambda_{low}^2\frac{\kappa_1}{\kappa_2}\frac{\rho_1^2}{\rho_2^2}}}{k_1\sqrt{\kappa_2}T_m\operatorname{erfc}\left(\lambda_{low}\sqrt{\frac{\kappa_1}{\kappa_2}\frac{\rho_1}{\rho_2}}\right)} = \frac{\lambda_{low}L\sqrt{\pi}}{c_1 T_m}\frac{\rho_2}{\rho_1} \tag{A18}$$

For the lower boundary, the region $y < 0$ is initially liquid and at constant temperature T_l, while the surface at $y = 0$ is maintained at air temperature T_a. The boundary conditions are in this case:

$$T_1 = T_a \qquad , \text{for } y = 0,\ t \geq 0 \tag{A19}$$

$$T_2 \to T_l \qquad , \text{for } y \to \infty,\ t \geq 0 \tag{A20}$$

$$T_1 = T_2 = T_m \qquad , \text{for } y = s(t),\ t \geq 0 \tag{A21}$$

Proceeding in a similar way the upper crust, its solution in the coordinate system of the right-hand side of Figure 11 is:

$$T_1(t) = T_a + \frac{T_m - T_a}{\operatorname{erf}(\lambda_{up})}\operatorname{erf}\frac{y}{2\sqrt{\kappa_1 t}} \tag{A22}$$

$$T_2(t) = T_l - \frac{T_l - T_m}{\operatorname{erfc}\left(\lambda_{up}\sqrt{\frac{\kappa_1}{\kappa_2}\frac{\rho_1}{\rho_2}}\right)} \operatorname{erfc}\left(\frac{y}{2\sqrt{\kappa_2 t}} + \frac{\lambda_{up}(\rho_1 - \rho_2)\sqrt{\kappa_1}}{\rho_2\sqrt{\kappa_2}}\right) \quad \text{(A23)}$$

$$\frac{e^{-\lambda^2}}{\operatorname{erf}(\lambda_{up})} - \frac{(T_l - T_m)k_2\sqrt{\kappa_1}e^{-\lambda_{up}^2\rho_1^2\kappa_1/\rho_2^2\kappa_2}}{(T_m - T_a)k_1\sqrt{\kappa_2}\operatorname{erfc}(\lambda_{up}\rho_1\sqrt{\kappa_1}/\rho_2\sqrt{\kappa_2})} = \frac{\lambda_{up}L\sqrt{\pi}}{c_1(T_m - T_a)} \quad \text{(A24)}$$

Note that λ_{low} for the lower crust is calculated from Equation A18, and λ_{up} for the upper crust from Equation A24. When combining these two solutions, the problem arises that the boundary conditions, $\lim_{y\to\infty} T_2 = T_l$, for the liquid phase are not valid any more. For simplicity, it is therefore assumed that the lava field is emplaced homogeneously at the melting point. Combining these solutions means flipping the upper crust along the x-axis and moving it by D in positive y-direction, i.e. replacing y in the solution for the upper crust by $D - y$.

In our case the lava flows are emplaced on older lava, thus the thermal properties of lava and substrate are assumed to be the same. In this situation, the temperature distribution of Equations A16 and A22 simplifies to:

$$T_{low}(t) = T_b + \frac{T_l - T_b}{\operatorname{erf}(\lambda_{low}) + 1} \cdot \left(1 + \operatorname{erf}\frac{y}{2\sqrt{\kappa t}}\right) \quad \text{, for } y \leq s_{low}(t) \quad \text{(A25)}$$

$$T_{up}(t) = T_a + \frac{T_l - T_a}{\operatorname{erf}\lambda_{up}} \operatorname{erf}\frac{D - y}{2\sqrt{\kappa t}} \quad \text{, for } y \geq s_{up}(t) \quad \text{(A26)}$$

L denotes latent heat, κ thermal diffusivity and c the specific heat of the lava. $s_{low}(t)$ and $s_{up}(t)$ are the positions of the solidification boundaries as in Equation A13. λ_{up} and λ_{low} are constants for the upper and lower crusts, which can be derived implicitly from Equations A18 and A24. In the case of uniform thermal properties these equations simplify to:

$$\frac{e^{-\lambda_{low}^2}}{1+\mathrm{erf}(\lambda_{low})} = \frac{\lambda_{low} L\sqrt{\pi}}{c\cdot(T_l - T_b)}\frac{\rho_{liq}}{\rho_{sol}} \tag{A27}$$

$$\frac{e^{-\lambda_{up}^2}}{\mathrm{erf}(\lambda_{up})} = \frac{\lambda_{up} L\sqrt{\pi}}{c\cdot(T_l - T_a)} \tag{A28}$$

ρ_{liq} and ρ_{sol} denote densities of the liquid and solid phase. The total contraction is a combination of thermal contraction and contraction related to phase change of crystallizing minerals. The latter is associated with density change from liquid to solid state of the lava.

Because of the density change during solidification, which occurs in either crust, the lava contracts at a velocity $u_{low} + u_{up}$, which can be derived from Equation A6. Additionally, the lava cools and thermal contraction occurs, so that the total vertical velocity u_{tot} of the lava surface is

$$u_{tot} = u_{low} + u_{up} + u_{th} \tag{A29}$$

with u_{th} denoting vertical velocity related to thermal contraction. The resulting volume change due to thermal contraction is calculated from equation 5 in main text.

One must keep track of the evolving thicknesses of the crusts to determine the time they meet. After this time of solidification, the two separated problems for the lower and upper crust must be merged together, as schematically shown in Figure 10.

$$\nabla^2 T = \frac{1}{\kappa}\frac{\partial T}{\partial t} \tag{A30}$$

The output of equations A25 - A28 form a unique temperature distribution dependent on thermal parameters (see Figure 12). Following the solidification process, heat is conducted away from the lava core according to eq. A30, under the assumption that k, κ and ρ are constants and that there is no internal heat generation.

Acknowledgments. The research leading to these results has received funding from the People Programme (Marie Curie Actions) of the European Union's Seventh Framework Programme (FP7/2007-2013) under the project NEMOH, REA grant agreement n° 289976. This project received also partial support from the European Community's Seventh Framework Programme (grant No 308377, project FUTUREVOLC). Y. Lavallée acknowledges funds from a Starting Grant on Strain Localisation in Magma (SLiM, no 306488) from the European Research Council. An intermediate TanDEM-X digital elevation model was provided by DLR under project IDEM_GEOL0123. COSMO-SkyMed data were provided by the Italian Space Agency (ASI) and ERS and Envisat data were provided by the European Space Agency (ESA) through the Icelandic Volcanoes Supersite project supported by the Committee on Earth Observing Satellites (CEOS). ERS and Envisat data from Iceland are available at Geohazard Supersites and Natural Laboratories web portal: http://eo-virtual-archive4.esa.int/?q=Iceland. For access to COSMO-SkyMed data used in this study, contact the Icelandic Volcanoes supersite point-of-contact Freysteinn Sigmundsson (fs@hi.is). We would like to thank Benedikt G. Ofeigsson and Halldor Geirsson for providing their expertise and experience on deformation of Hekla volcano. Andy Hooper, Ian Hamling, Vincent Drouin, Michelle Parks and Jorge Montalvo were of great help for creation and interpretation of interferograms and additional data. Many thanks go as well to Chris Bean and Ivan Lokmer for providing possibilities of a secondment at UCD Dublin, and to Sigrun Hreinsdottir for the possibility of collaboration with GNS Science in Lower Hutt/New Zealand.

References

Briole, P., D. Massonnet, and C. Delacourt (1997), Post-eruptive deformation associated with the 1986–87 and 1989 lava flows of Etna detected by radar interferometry, *Geophysical Research Letters*, *24*(1), 37–40, doi:10.1029/96GL03705.

Byrd, R. H., P. Lu, J. Nocedal, and C. Zhu (1995), A limited memory algorithm for bound constrained optimization, *SIAM Journal on Scientific Computing*, *16*(5), 1190–1208, doi:10.1137/0916069.

Caricchi, L., J. Biggs, C. Annen, and S. Ebmeier (2014), The influence of cooling, crystallisation and re-melting on the interpretation of geodetic signals in volcanic systems, *Earth and Planetary Science Letters*, *388*(0), 166 – 174, doi: http://dx.doi.org/10.1016/j.epsl.2013.12.002.

Carslaw, H. S., and J. C. Jaeger (1959), *Conduction of heat in solids*, 2 ed., Oxford University Press Inc., New York.

Chaussard, E. (2016), Subsidence in the Parícutin lava field: Causes and implications for interpretation of deformation fields at volcanoes, *Journal of Volcanology and Geothermal Research*, *320*, 1 – 11, doi:http://dx.doi.org/10.1016/j.jvolgeores.2016.04.009.

Christensen, E. L., N. Skou, J. Dall, K. W. Woelders, J. H. Jorgensen, J. Granholm, and S. N. Madsen (1998), Emisar: an absolutely calibrated polarimetric l- and c-band sar, *IEEE Transactions on Geoscience and Remote Sensing*, *36*(6), 1852–1865, doi: 10.1109/36.729356.

Crank, J. (1984), *Free and moving boundary problems*, x, 425 p. : pp., Oxford University Press Inc., New York.

Dietterich, H. R., M. P. Poland, D. A. Schmidt, K. V. Cashman, D. R. Sherrod, and A. T. Espinosa (2012), Tracking lava flow emplacement on the east rift zone of Kilauea, Hawai'i, with Synthetic Aperture Radar coherence, *Geochemistry, Geophysics, Geosystems*, *13*(5), doi:10.1029/2011GC004016.

Ebmeier, S., J. Biggs, T. Mather, J. Elliott, G. Wadge, and F. Amelung (2012), Measuring large topographic change with InSAR: Lava thicknesses, extrusion rate and subsidence rate at Santiaguito volcano, Guatemala, *Earth and Planetary Science Letters*, *335–336*(0), 216 – 225, doi:http://dx.doi.org/10.1016/j.epsl.2012.04.027.

Einarsson, P., S. Björnsson, G. Foulger, R. Stefánsson, and T. Skaftadóttir (1981), *Seismicity Pattern in the South Iceland Seismic Zone*, pp. 141–151, American Geophysical Union, doi:10.1029/ME004p0141.

Geirsson, H., P. LaFemina, T. Árnadóttir, E. Sturkell, F. Sigmundsson, M. Travis, P. Schmidt, B. Lund, S. Hreinsdóttir, and R. Bennett (2012), Volcano deformation at active plate boundaries: Deep magma accumulation at Hekla volcano and plate boundary deformation in south Iceland, *Journal of Geophysical Research: Solid Earth*, *117*(B11), n/a–n/a, doi:10.1029/2012JB009400.

Ghiorso, M. S., M. M. Hirschmann, P. W. Reiners, and V. C. Kress (2002), The pmelts: A revision of melts for improved calculation of phase relations and major element partitioning related to partial melting of the mantle to 3 GPa, *Geochemistry, Geophysics, Geosystems*, *3*(5), 1–35, doi:10.1029/2001GC000217.

Grapenthin, R., B. G. Ófeigsson, F. Sigmundsson, E. Sturkell, and A. Hooper (2010), Pressure sources versus surface loads: Analyzing volcano deformation signal composition with an application to Hekla volcano, Iceland, *Geophysical Research Letters*, *37*(20), doi:10.1029/2010GL044590.

Gronvold, K., G. Larsen, P. Einarsson, S. Thorarinsson, and K. Saemundsson (1983), The Hekla eruption 1980–1981, *Bulletin Volcanologique*, *46*(4), 349–363, doi:10.1007/BF02597770.

Gudmundsson, A., N. Oskarsson, K. Gronvold, K. Saemundsson, O. Sigurdsson, R. Stefansson, S. R. Gislason, P. Einarsson, B. Brandsdottir, G. Larsen, H. Johannesson, and T. Thordarson (1992), The 1991 eruption of Hekla, Iceland, *Bulletin of Volcanology*, *54*(3), 238–246, doi:10.1007/BF00278391.

Hardee, H. C. (1980), Solidification in Kilauea Iki lava lake, *Journal of Volcanology and Geothermal Research*, *7*(3), 211 – 223, doi:http://dx.doi.org/10.1016/0377-0273(80)90030-X.

Harris, A. J., and S. Rowland (2001), Flowgo: a kinematic thermo-rheological model for lava flowing in a channel, *Bulletin of Volcanology*, *63*(1), 20–44, doi:10.1007/s004450000120.

Hooper, A. (2008), A multi-temporal insar method incorporating both persistent scatterer and small baseline approaches, *Geophysical Research Letters*, *35*(16), n/a–n/a, doi:10.1029/2008GL034654.

Hooper, A., H. Zebker, P. Segall, and B. Kampes (2004), A new method for measuring deformation on volcanoes and other natural terrains using insar persistent scatterers, *Geophysical Research Letters*, *31*(23), n/a–n/a, doi:10.1029/2004GL021737, l23611.

Hooper, A., D. Bekaert, K. Spaans, and M. Arikan (2012), Recent advances in SAR interferometry time series analysis for measuring crustal deformation, *Tectonophysics*, *514–517*, 1 – 13, doi:http://dx.doi.org/10.1016/j.tecto.2011.10.013.

Höskuldsson, Á., N. Óskarsson, R. Pedersen, K. Grönvold, K. Vogfjörd, and R. Ólafsdóttir (2007), The millennium eruption of Hekla in February 2000, *Bulletin of Volcanology*, *70*(2), 169–182, doi:10.1007/s00445-007-0128-3.

Kampes, B., and S. Usai (1999), Doris: The delft object-oriented radar interferometric software, Proceedings ITC 2nd ORS symposium.

Kattenhorn, S. A., and C. J. Schaefer (2008), Thermal–mechanical modeling of cooling history and fracture development in inflationary basalt lava flows, *Journal of Volcanology and Geothermal Research*, *170*(3–4), 181 – 197, doi: http://dx.doi.org/10.1016/j.jvolgeores.2007.10.002.

Keiding, M., T. Árnadóttir, S. Jónsson, J. Decriem, and A. Hooper (2010), Plate boundary deformation and man-made subsidence around geothermal fields on the reykjanes peninsula, iceland, *Journal of Volcanology and Geothermal Research*, *194*(4), 139 – 149, doi:http://dx.doi.org/10.1016/j.jvolgeores.2010.04.011.

Keszthelyi, L. (1994), Calculated effect of vesicles on the thermal properties of cooling basaltic lava flows, *Journal of Volcanology and Geothermal Research*, *63*(3–4), 257 – 266, doi:http://dx.doi.org/10.1016/0377-0273(94)90078-7.

Lange, R., K. Cashman, and A. Navrotsky (1994), Direct measurements of latent heat during crystallization and melting of a ugandite and an olivine basalt, *Contributions to Mineralogy and Petrology*, *118*(2), 169–181, doi:10.1007/BF01052867.

Lu, Z., T. Masterlark, and D. Dzurisin (2005), Interferometric Synthetic Aperture Radar study of Okmok volcano, Alaska, 1992–2003: Magma supply dynamics and postemplacement lava flow deformation, *Journal of Geophysical Research: Solid Earth*, *110*(B2), doi:10.1029/2004JB003148, b02403.

Lu, Z., D. Dzurisin, J. Biggs, C. Wicks Jr., and S. McNutt (2010), Ground surface deformation patterns, magma supply, and magma storage at Okmok volcano, Alaska, from InSAR analysis: 1. intereruption deformation, 1997–2008, *Journal of Geophysical Research*, *115*, doi:10.1029/2009JB006969.

Magnússon, E. (2003), Airborne sar data from S-Iceland: analyses, dem improvements and glaciological application, Master's thesis, University of Iceland.

Massonnet, D., and K. L. Feigl (1998), Radar interferometry and its application to changes in the earth's surface, *Reviews of Geophysics*, *36*(4), 441–500, doi:10.1029/97RG03139.

Moune, S., P.-J. Gauthier, S. R. Gislason, and O. Sigmarsson (2006), Trace element degassing and enrichment in the eruptive plume of the 2000 eruption of Hekla volcano, Iceland, *Geochimica et Cosmochimica Acta*, *70*(2), 461–479, doi: http://dx.doi.org/10.1016/j.gca.2005.09.011.

Ofeigsson, B. G., A. Hooper, F. Sigmundsson, E. Sturkell, and R. Grapenthin (2011), Deep magma storage at Hekla volcano, Iceland, revealed by InSAR time series analysis, *Journal of Geophysical Research: Solid Earth*, *116*(B5), doi:10.1029/2010JB007576.

Patrick, M. R., J. Dehn, and K. Dean (2004), Numerical modeling of lava flow cooling applied to the 1997 Okmok eruption: Approach and analysis, *Journal of Geophysical Research: Solid Earth*, *109*(B3), doi:10.1029/2003JB002537, b03202.

Peck, D. L. (1978), Cooling and vesiculation of Alae lava lake, Hawaii, *Tech. rep.*, U. S. Govt. Print. Off.

Pedersen, G., J. M.-C. Belart, O. K. Vilmundardóttir, N. Falco, F. S. Sigurmundsson, R. Rustowicz, S. Tarquini, M. de' Michieli Vitturi, G. Gísladóttir, and J. A. Benediktsson (2016), The landscape evolution at Hekla volcano, Iceland: Integrating remote sensing data from the past 70yr, in *Geophysical Research Abstracts*, vol. 18, EGU General Assembly 2016.

Rosen, P. A., S. Hensley, I. R. Joughin, F. K. Li, S. N. Madsen, S. Member, E. Rodríguez, and R. M. Goldstein (2000), Synthetic Aperture Radar interferometry, in *Proceedings of the IEEE*, pp. 333–382.

Shaw, H. R., M. S. Hamilton, and D. L. Peck (1977), Numerical analysis of lava lake cooling models; part i, description of the method, *American Journal of Science*, *277*(4), 384–414.

Sigmundsson, F., P. Einarsson, R. Bilham, and E. Sturkell (1995), Rift-transform kinematics in south Iceland: Deformation from Global Positioning System measurements, 1986 to 1992, *Journal of Geophysical Research: Solid Earth*, *100*(B4), 6235–6248, doi:10.1029/95JB00155.

Sigmundsson, F., H. Vadon, and D. Massonnet (1997), Readjustment of the Krafla spreading segment to crustal rifting measured by satellite radar interferometry, *Geophysical Research Letters*, *24*(15), 1843–1846, doi:10.1029/97GL01934.

Stevens, N. F., G. Wadge, and C. A. Williams (2001a), Post-emplacement lava subsidence and the accuracy of ERS InSAR digital elevation models of volcanoes, *International Journal of Remote Sensing*, *22*(5), 819–828, doi:10.1080/01431160051060246.

Stevens, N. F., G. Wadge, C. A. Williams, J. G. Morley, J.-P. Muller, J. B. Murray, and M. Upton (2001b), Surface movements of emplaced lava flows measured by Synthetic Aperture Radar interferometry, *Journal of Geophysical Research: Solid Earth*, *106*(B6), 11,293–11,313, doi:10.1029/2000JB900425.

Thorarinsson, S. (1950), The eruption of Mt. Hekla 1947 – 1948, *Bulletin Volcanologique*, *10*(1), 157–168, doi:10.1007/BF02596085.

Turcotte, D. L., and G. Schubert (2002), *Geodynamics*, 2nd ed., Cambridge University Press.

Wright, T. J., B. E. Parsons, and Z. Lu (2004), Toward mapping surface deformation in three dimensions using InSAR, *Geophysical Research Letters*, *31*(1), doi: 10.1029/2003GL018827, l01607.

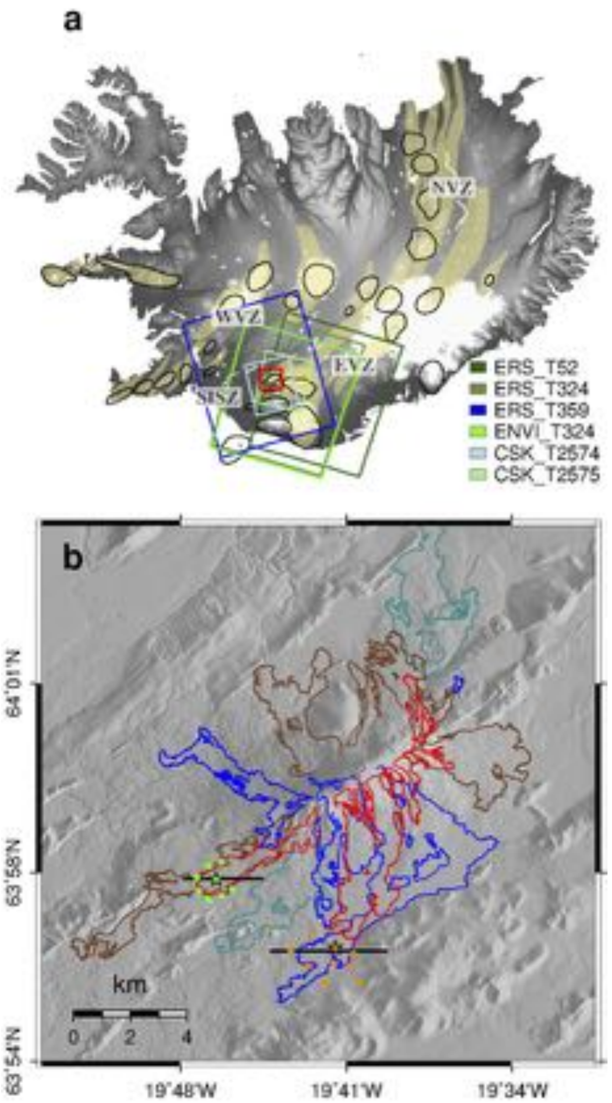

Figure 1. **(a)** Shaded relief map of Iceland with glaciers in white, fissure swarms in yellow and outlines of central volcanoes in black. SAR images from satellite tracks in ascending configuration are shown as blue rectangles and in descending configuration as green rectangles. A red rectangular shows the zoom region of (b) covering Hekla volcano. **(b)** Shaded relief map of Hekla volcano (center of map) with outlines of recent lava flows (1970: turquoise, 1980/1981: brown, 1991: blue, 2000: red).

Dots encompass two lava tongues which are the focus of this study. Orange circles show the reference areas for part of the 1991 lava field, with the orange star marking the sample area on the lava field. Green dots show the reference areas for the 2000 lava field, with the green star marking the sample area on the lava field. Radii are 100 m for all areas. Black lines mark profiles crossing the 1991 and 2000 lava fields shown in Figure 4.

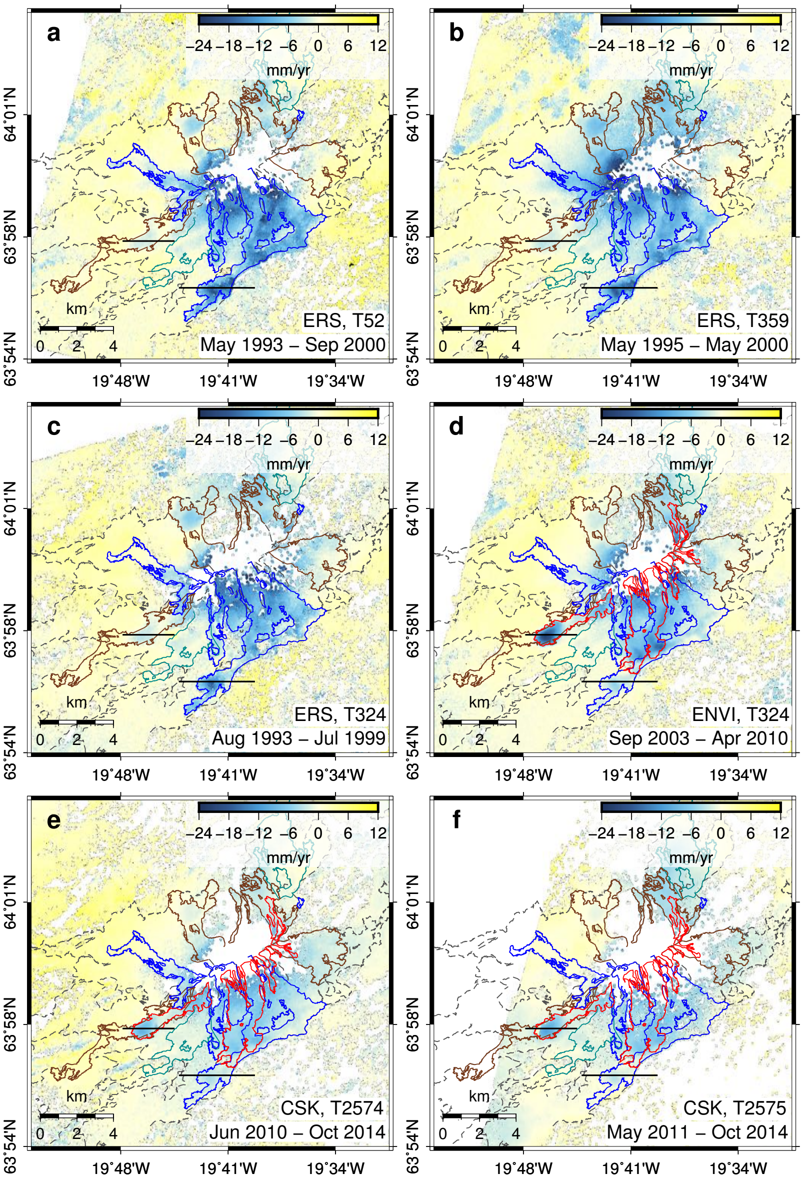

Figure 2. Average LOS velocities calculated from time series shown in Appendix 1. The panels display a zoom of the LOS velocity fields, with Hekla in the center. White corresponds to areas without data, including areas were no data were acquired and incoherent areas. Blue corresponds to LOS lengthening, orange to LOS shortening. Outlines of recent lava flows (1970: turquoise, 1980/1981: brown, 1991: blue, 2000: red). **(a)** Descending ERS Track 52 from 25/05/1993 to 29/09/2000, **(b)** Descending ERS Track 324 from 06/05/1995 to 31/05/2000, **(c)** Ascending ERS Track 359 from 24/08/1993 to 23/07/1999, **(d)** Descending Envisat Track 324 from 03/09/2003 to 14/04/2010, **(e)** Ascending CSK Track 2574 from 18/06/2010 to 11/10/2014, **(f)** Descending CSK Track 2575 from 19/05/2011 to 16/10/2014.

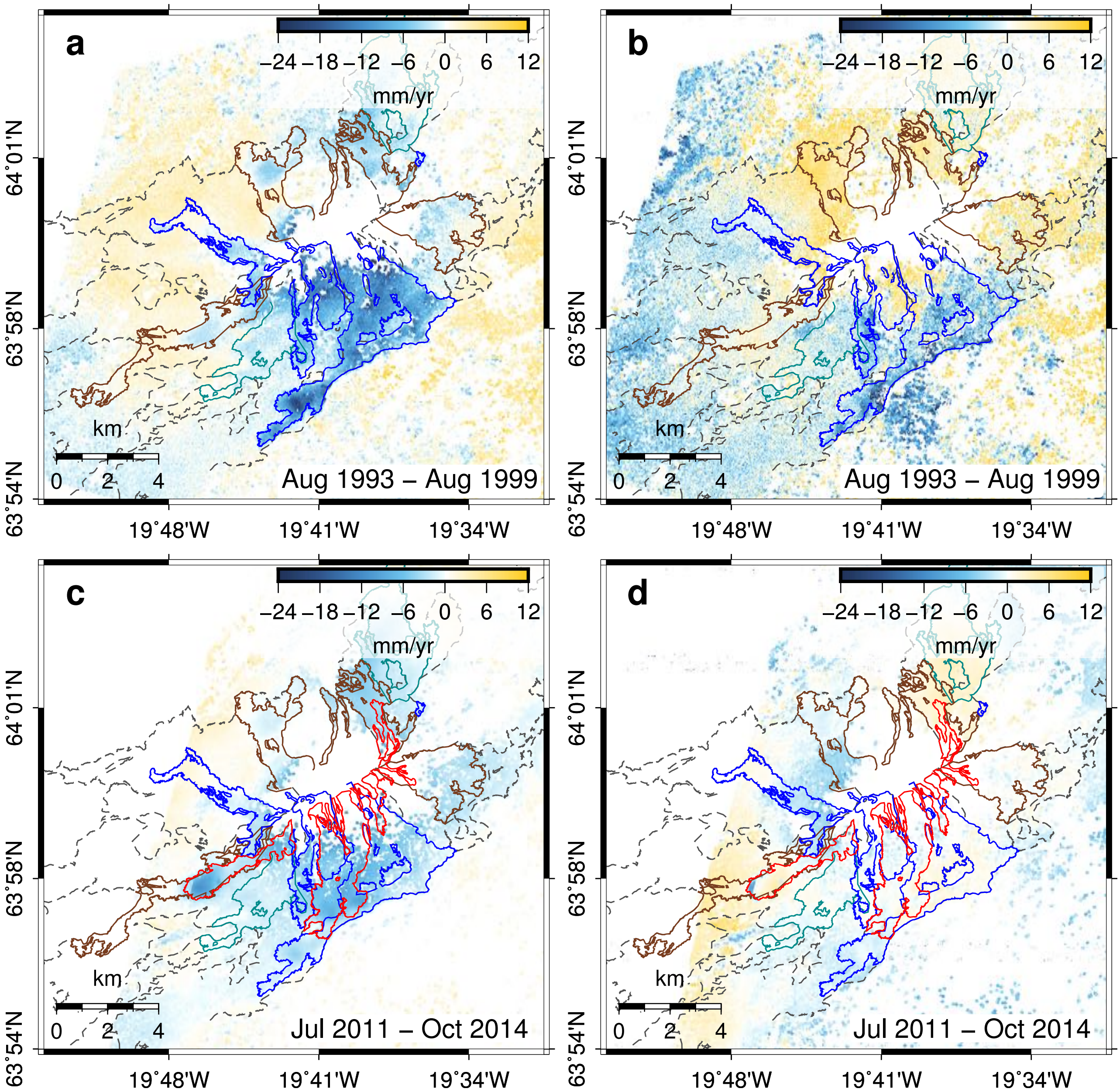

Figure 3. Linear combinations of LOS changes in ascending and descending ERS and CSK tracks. **(a)** Sum of LOS velocity fields from descending ERS Track 52 and ascending ERS Track T359, normalized to reveal near-vertical displacement. **(b)** The corresponding difference, normalized to reveal approximate east displacement. **(c)** Sum of LOS velocity fields from of ascending CSK Track 2574 and descending CSK Track T2575 normalized to reveal near-vertical displacement. **(d)** The corresponding difference, normalized reveal approximate east displacement.

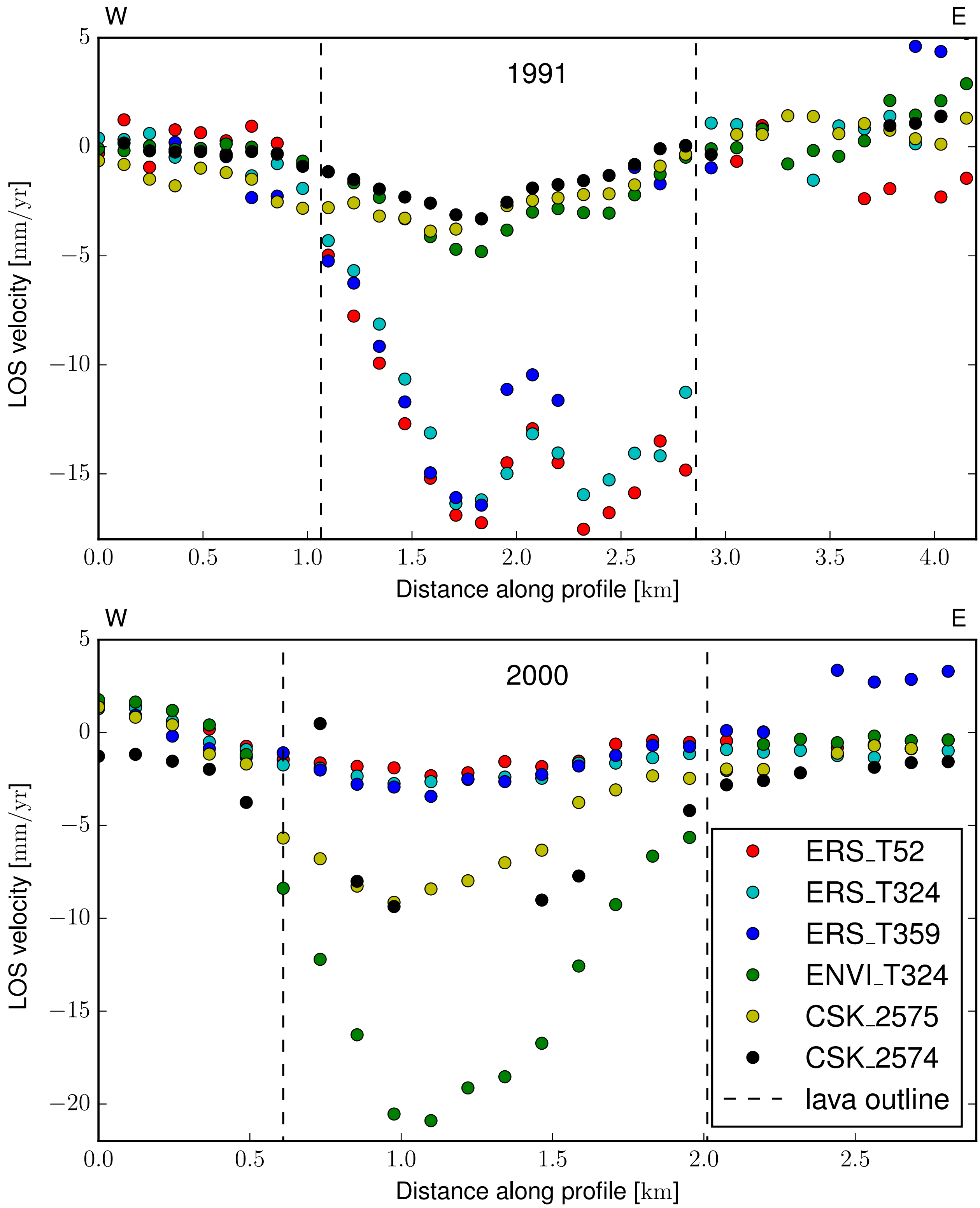

Figure 4. LOS velocity profiles across lava tongues. Distance along profiles (see black lines in Figure 1) are from west to east. The upper figure shows the profile through the 1991 lava tongue. The lower figure shows the profile through the 2000 lava tongue. Vertical dashed lines show the lateral extent of the lava tongues along each profile.

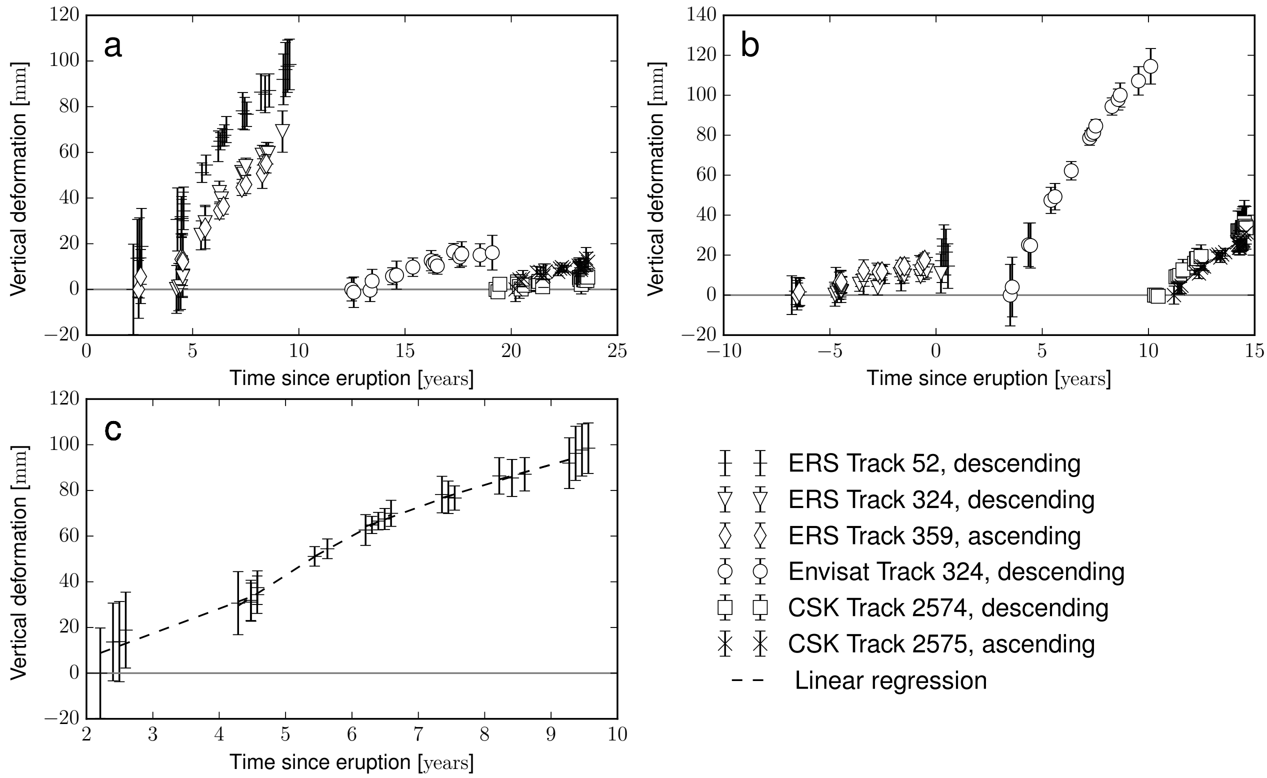

Figure 5. Inferred vertical change (subsidence is positive) and linear regression. **(a)** Inferred vertical deformation of the sample area of the 1991 Hekla lava tongue relative to surrounding area. **(b)** Inferred vertical deformation of the sample area of the 2000 Hekla lava tongue relative to surrounding area. A linear trend before the eruption ($t = 0$ years) is noticeable. **(c)** Example of linear regression for ERS Track 52. The slopes of the individual regressions yield the vertical velocities for each time span.

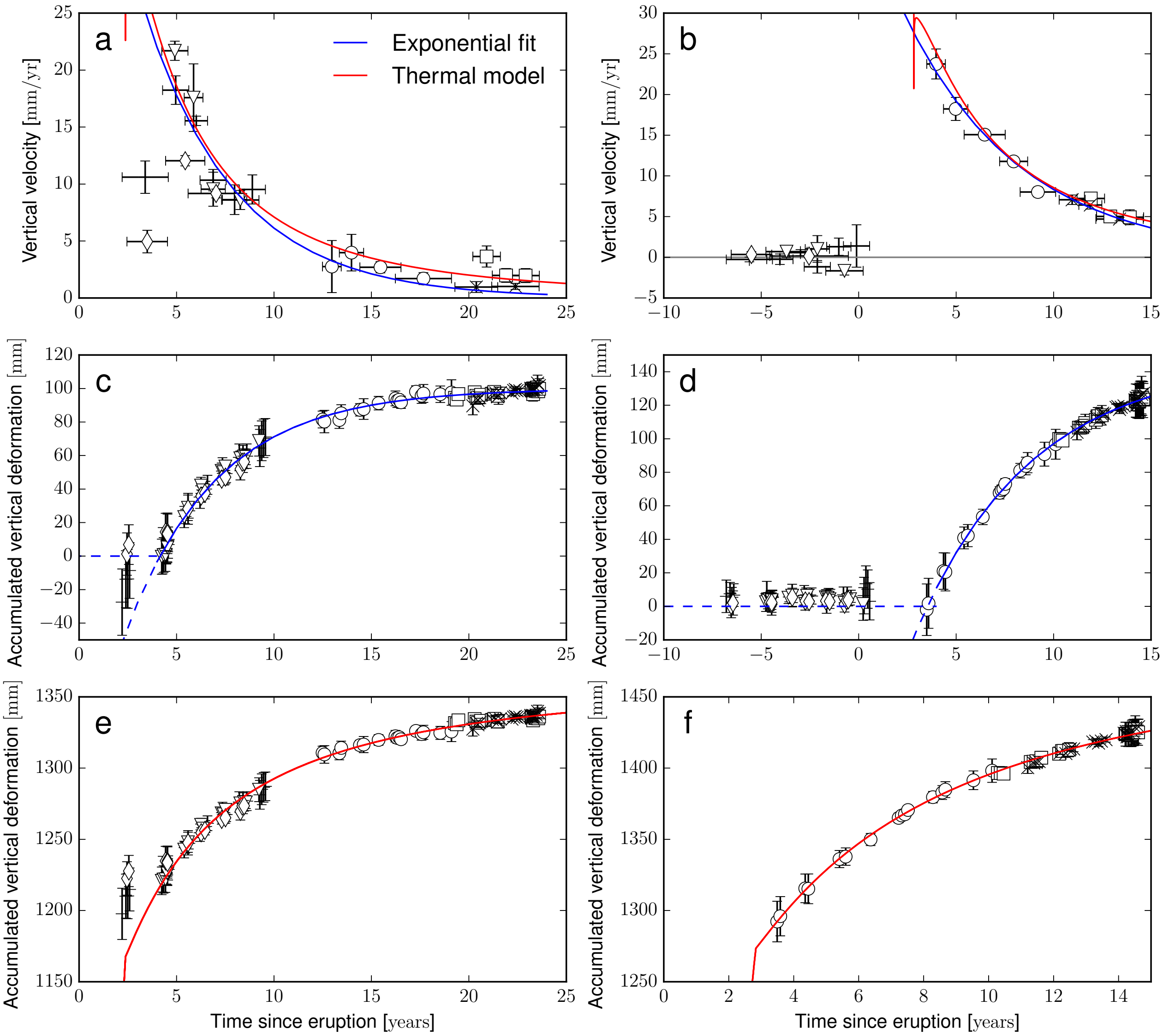

Figure 6. Inferred vertical velocity and deformation (subsidence is positive) **(a)** Vertical surface velocity of 1991 lava tongue relative to surrounding area and best fitting models. **(b)** Vertical surface velocity of 2000 lava tongue relative to surrounding area and best fitting models. **(c)** Exponential fit for accumulated vertical deformation of 1991 lava tongue. **(d)** Exponential fit for accumulated vertical deformation of 2000 lava tongue. **(e)** Best fitting thermal model for accumulated vertical deformation of 1991 lava tongue. **(f)** Best fitting thermal model for accumulated vertical deformation of 2000 lava tongue.

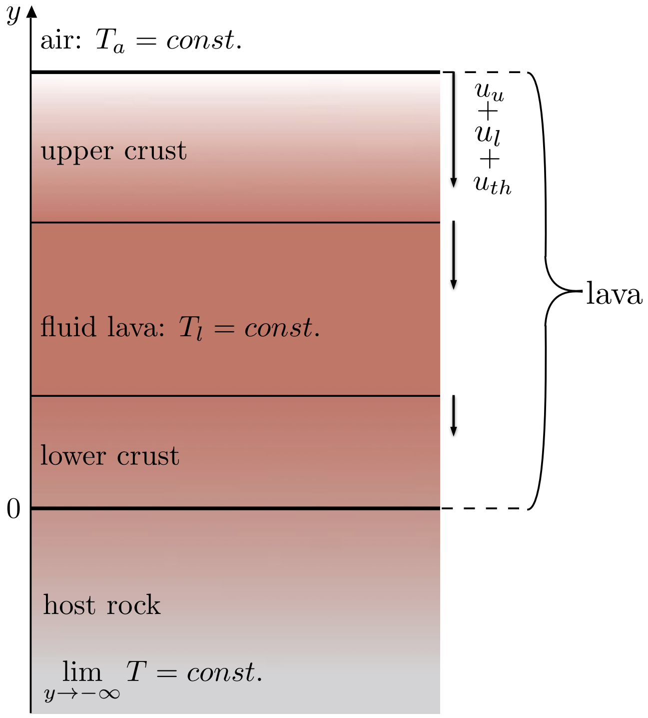

Figure 7. Scheme of the thermal model. A lava flow is emplaced at temperature T_l and heat is conducted away into the air and bed rock. The upper surface of the flow moves at a velocity $u_{up} + u_{low} + u_{th}$, due to density changes during phase transition and cooling.

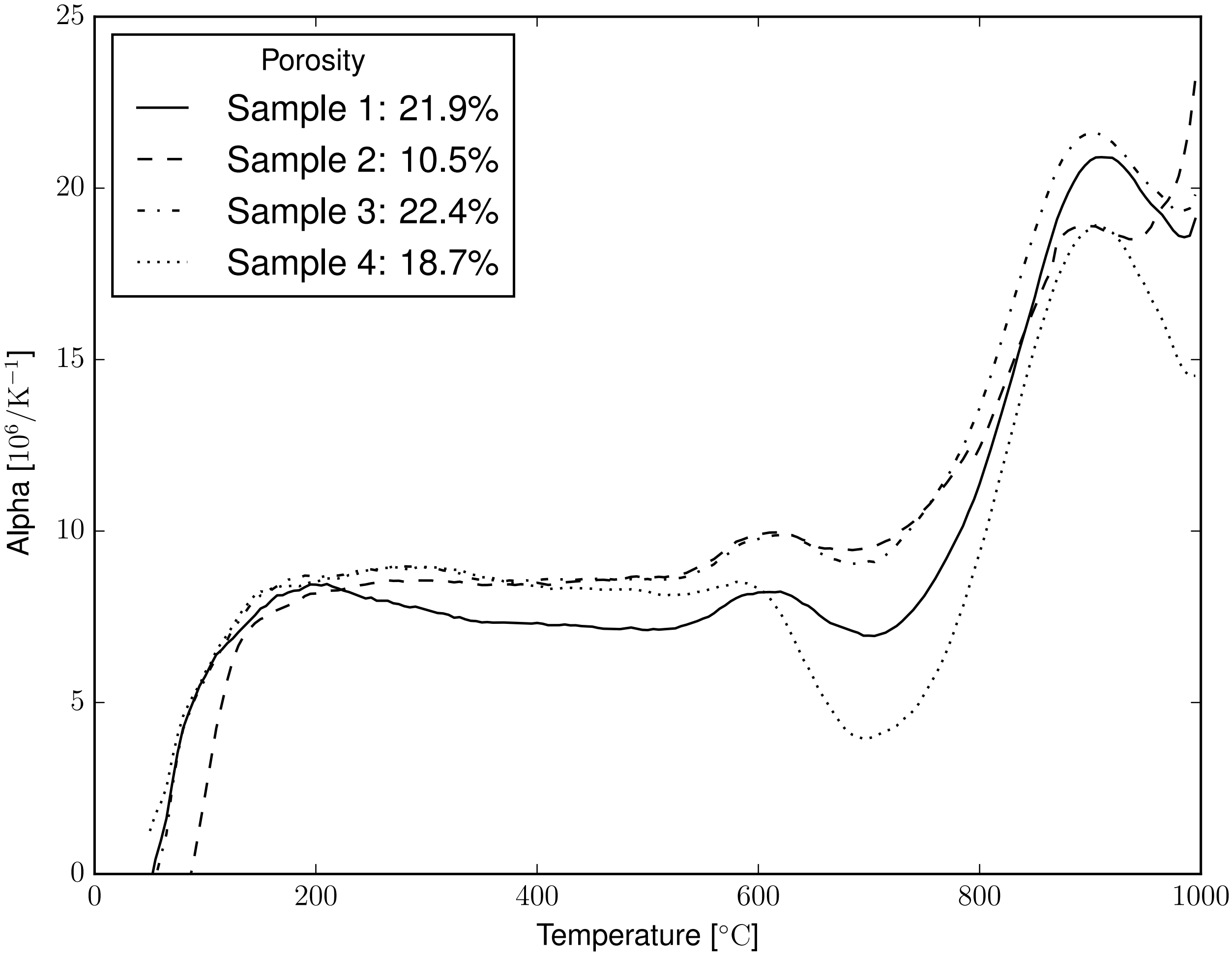

Figure 8. Expansion coefficient of 2000 Hekla lava tongue as a function of temperature. Data below $\approx$ 150°C highlight the initial thermal adjustment of the furnace and sample assembly. The data shows that the expansion coefficient is constant between 200 and $600 - 700$°C for all samples. Above this temperature we note an increase in thermal expansivity and a peak due to partial melting at circa 980°C, which mechanically results in softening of the sample.

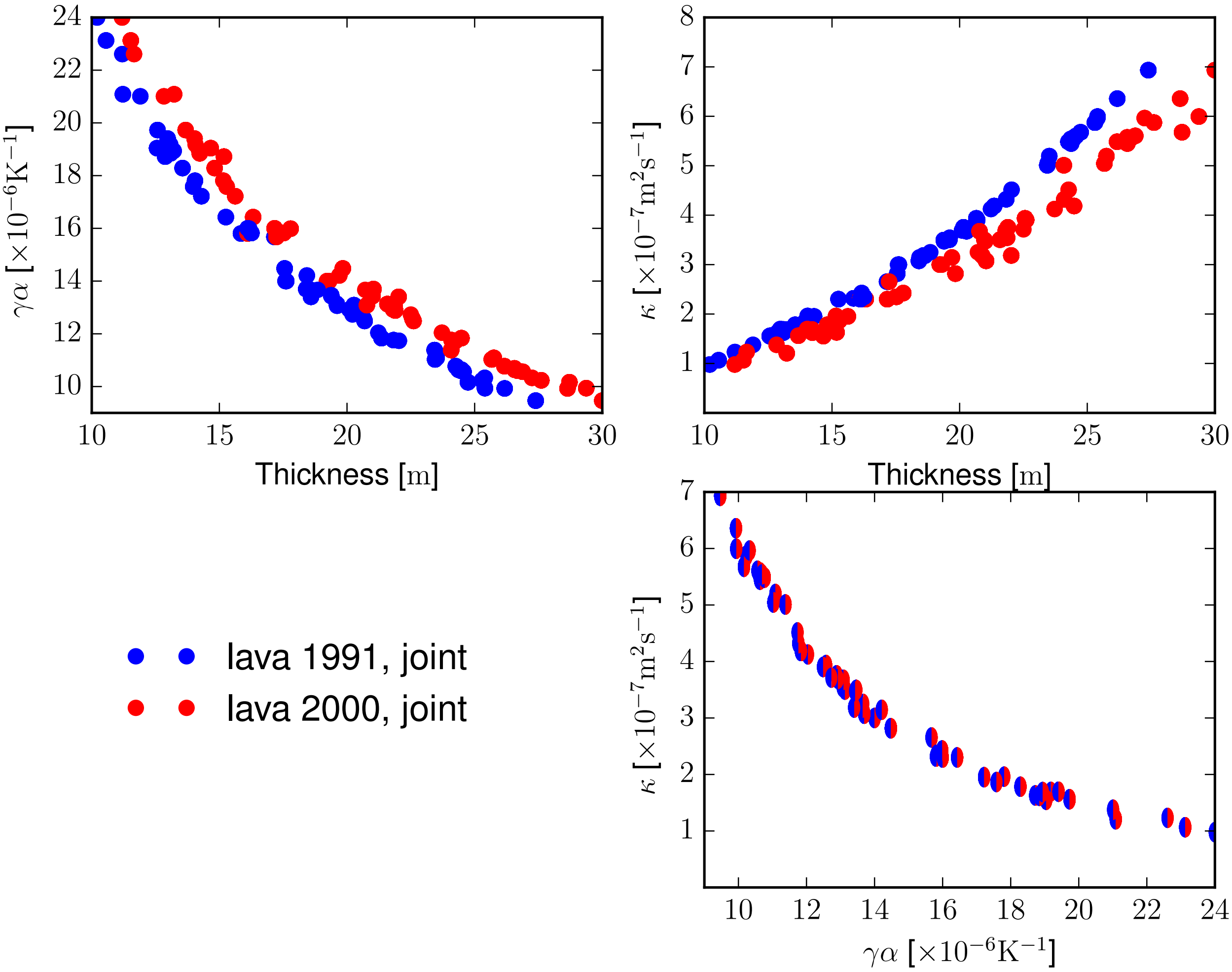

Figure 9. Cross-correlation between pairs of parameters of the joint inversion. Each point represents a single solution of the inversion. All the points on the plots result in a similar residual between models and observations and lead to root-mean-square errors of about 1.53 mm/yr. Blue dots refer to the 1991 lava tongue, and red dots to the 2000 lava tongue. The inversion process seeks to minimize the standard deviation between the thermal model and measured subsidence rates (see Figures 6a and b). Parameters are initial thicknesses of the 1991 and 2000 lava tongues, effective vertical thermal expansivity, $\gamma\alpha$, and thermal diffusivity, κ. Latent heat L and specific heat c were kept constant at $L = 320 \times 10^3$ Jkg^{-1} and $c = 1200$ Jkg^{-1}K^{-1}, respectively.

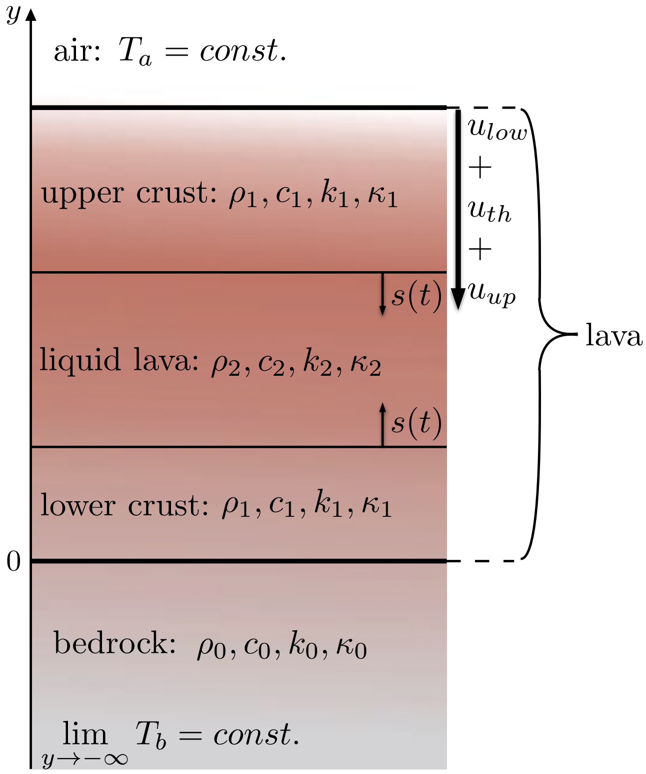

Figure 10. Scheme of the model. Indices 0 refer to bedrock, 1 to solidified lava and 2 to fluid lava. Thus, the bedrock may have different properties than the solidified lava. For explanation see text.

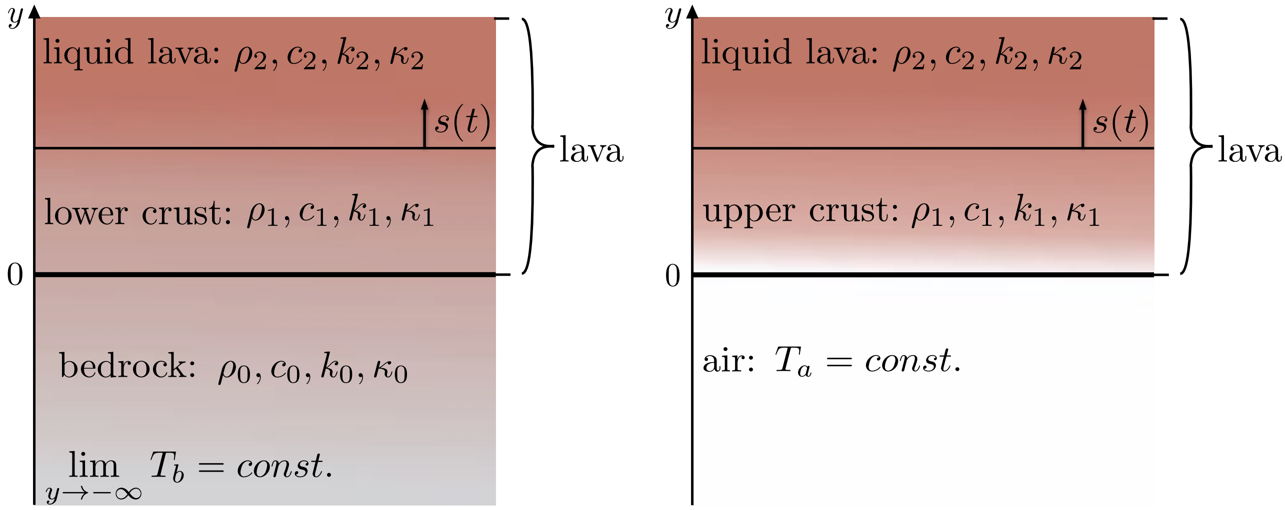

Figure 11. Solving the model as two separate problems for the lower (left-hand side) and upper (right-hand side) crust. Afterwards, the problem is merged back into the original problem by mirroring the coordinate system for the upper crust along the x-axis.

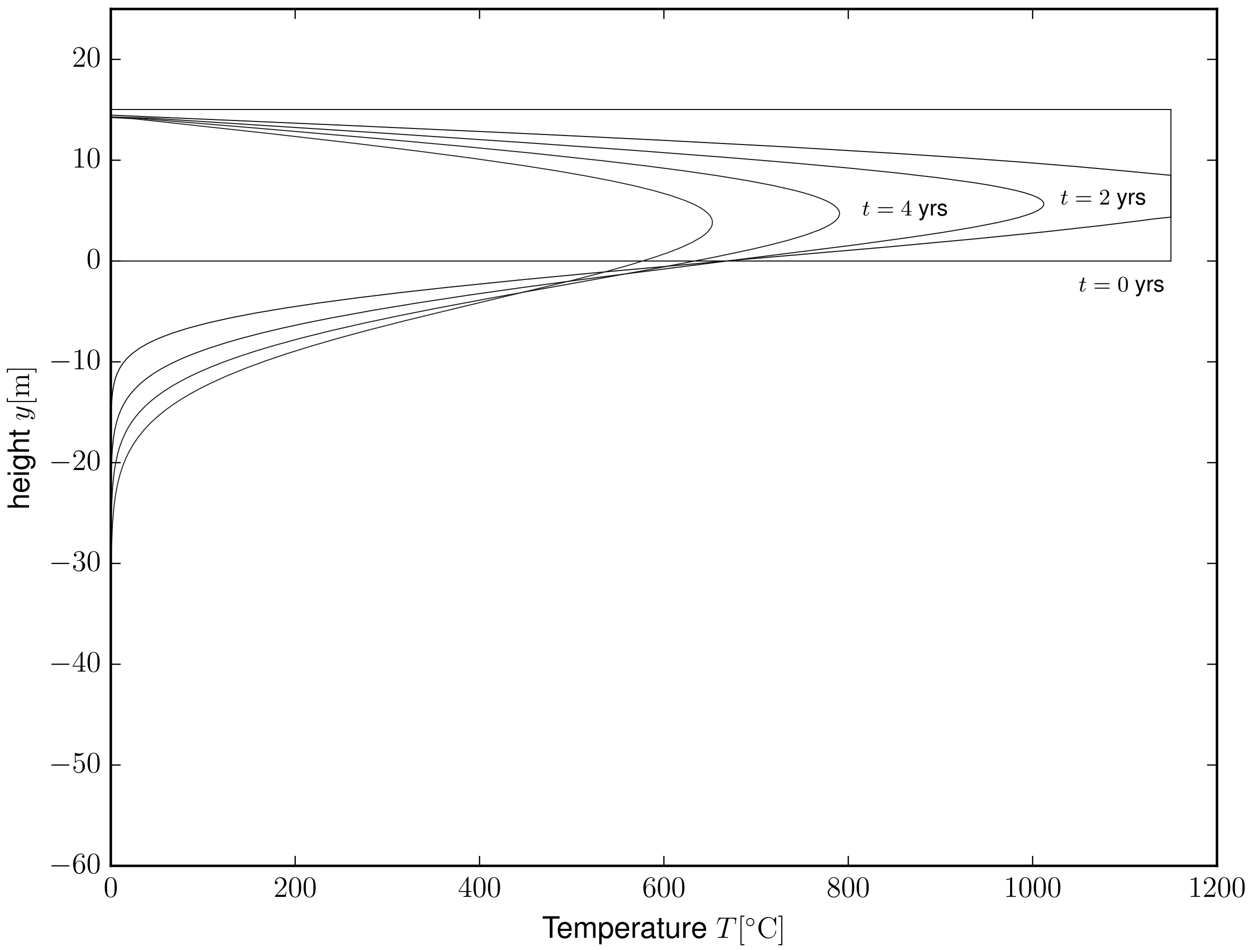

Figure 12. Time evolution of the temperature distribution. The rectangle represents the initial distribution at $t = 0$ years with a lava thickness of 15.00 m. A scaled thermal expansivity value of $\gamma \cdot \alpha = 1.66 \times 10^{-5}\mathrm{K}^{-1}$ and a thermal diffusivity value of $\kappa = 3.00 \times 10^{-7}\mathrm{m}^2\mathrm{s}^{-1}$ has been used (compare Section 4.2). The temperature distribution is plotted every year of simulation time. The upper and lower crusts meet at $t = 1.67$ yrs, the time of full solidification. Note the decreasing thickness of the lava (the upper intersection of the curves with the y-axis).

Table 1. Satellite data and time span of acquisitions.

Satellite	Track	Time span	Geometry	Incidence angle	LOS unit vector (Up/N/E)	Figure
ERS	52	05/1993 - 09/2000	descending	24.7°	(0.92/-0.13/0.35)	S1
	324	05/1995 - 05/2000	descending	22.3°	(0.93/-0.14/0.35)	S2
	359	08/1993 - 07/1999	ascending	22.0°	(0.94/-0.12/-0.31)	S3
Envisat	324	09.2003 - 04/2010	descending	22.3°	(0.93/-0.14/0.35)	S4
CSK	2574	06/2010 - 10/2014	ascending	32.2°	(0.85/-0.17/-0.5)	S5
	2575	05/2011 - 10/2014	descending	23.9°	(0.91/-0.14/0.38)	S6

Table 2. Table of parameters

Parameter name	Symbol	Value* [SI]	Literature	comment
Density of solid lava	ρ_{sol}	1660 - 2780	[*Peck*, 1978]	Alae, Hawaii
		2799	MELTS	Hekla (1991, 2000)
Density of liquid lava	ρ_{liq}	(2790 ± 30), 2740	[*Peck*, 1978]	Alae, Hawaii
		2654	MELTS	Hekla lava (1991)
		2663	MELTS	Hekla lava (2000)
Thermal expansivity	α	8.3×10^{-6}	Laboratory	Hekla lava (1991)
		$(3 \pm 1) \times 10^{-6}$	[*Peck*, 1978]	Alae, Hawaii
Thermal diffusivity	κ	$5 \cdots 6 \times 10^{-7}$	[*Peck*, 1978]	Alae, Hawaii
Latent heat of fusion	L	$(335 \pm 42) \times 10^{3}$	[*Peck*, 1978]	Alae, Hawaii
Specific heat	c	$0.75 \cdots 1.23 \times 10^{3}$	[*Peck*, 1978]	Alae, Hawaii

* All numerical values are given in corresponding SI-units.

Table 3. *A priori* values of parameters used in the inversion

Parameter name	Symbol	*A priori* range	
Initial thickness (1991)	D_{1991}	$8 \cdots 30$	m
Initial thickness (2000)	D_{2000}	$8 \cdots 30$	m
Thermal expansion	α	8.3×10^{-6}	K^{-1}
Scaling coefficient	γ	$0.25 \cdots 3$	
Thermal diffusivity	κ	$0.5 \cdots 9 \times 10^{-7}$	m^2s^{-1}
Latent heat of fusion	L	320×10^{3}	Jkg^{-1}
Specific heat	c	1.2×10^{3}	$Jkg^{-1}K^{-1}$

Supporting Information for "Post-emplacement cooling and contraction of lava flows: InSAR observations and a thermal model for lava fields at Hekla volcano, Iceland"

DOI: 10.1002/

Werner Wittmann[1], Freysteinn Sigmundsson[1]

Stéphanie Dumont[1], Yan Lavallée[2],

Corresponding author: W. Wittmann, Institute of Earth Sciences, University of Iceland, Sturlugata 7, Reykjavík IS-101, Iceland. (wew1@hi.is)

[1]Nordic Volcanological Center, Institute of Earth Sciences, University of Iceland, Reykjavík, IS-101 Iceland

[2]Department of Earth, Ocean and Ecological Sciences, University of Liverpool, Liverpool L69 3GP, UK

Additional Supporting Information: InSAR time series

1. Figure 1: ERS Track 52
2. Figure 2: ERS Track 324
3. Figure 3: ERS Track 359
4. Figure 4: Envisat Track 324
5. Figure 5: CSK Track 2574
6. Figure 6: CSK Track 2575

Introduction

All InSAR time series shown in this supporting information were processed using the StaMPS processing software *Hooper et al.* [2012]. The data points result from a merged processing approach, combining both permanent scatterer and small baseline approaches in the interferometric analysis. Furthermore, ramps in the interferograms were removed. Table 1 shows the satellites and the time span of the data used. Figures S1 through S6 show the corresponding time series.

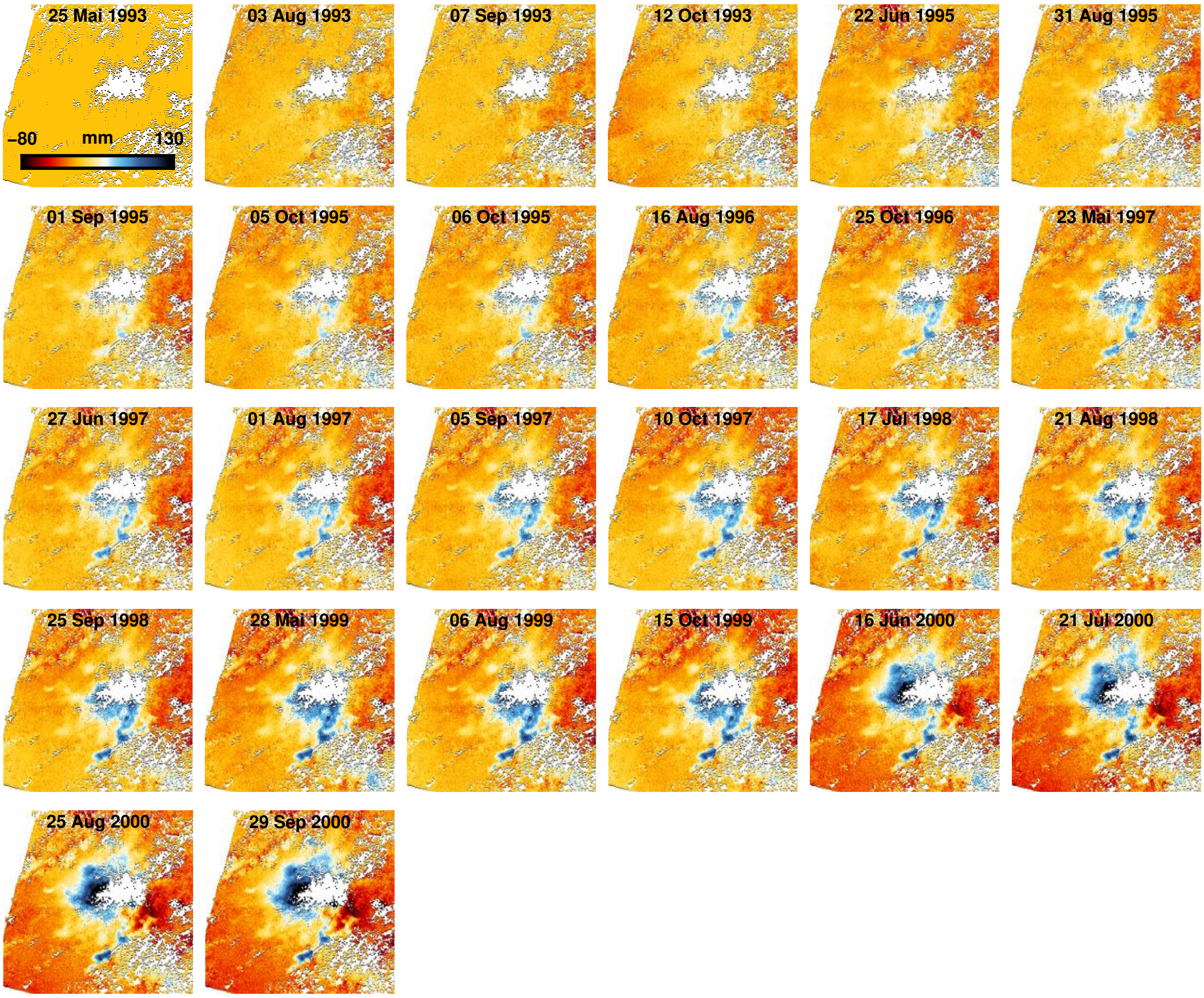

Figure S1. ERS time series spanning 1993 to 2000. Accumulated LOS unwrapped phase change, Track 52, descending.

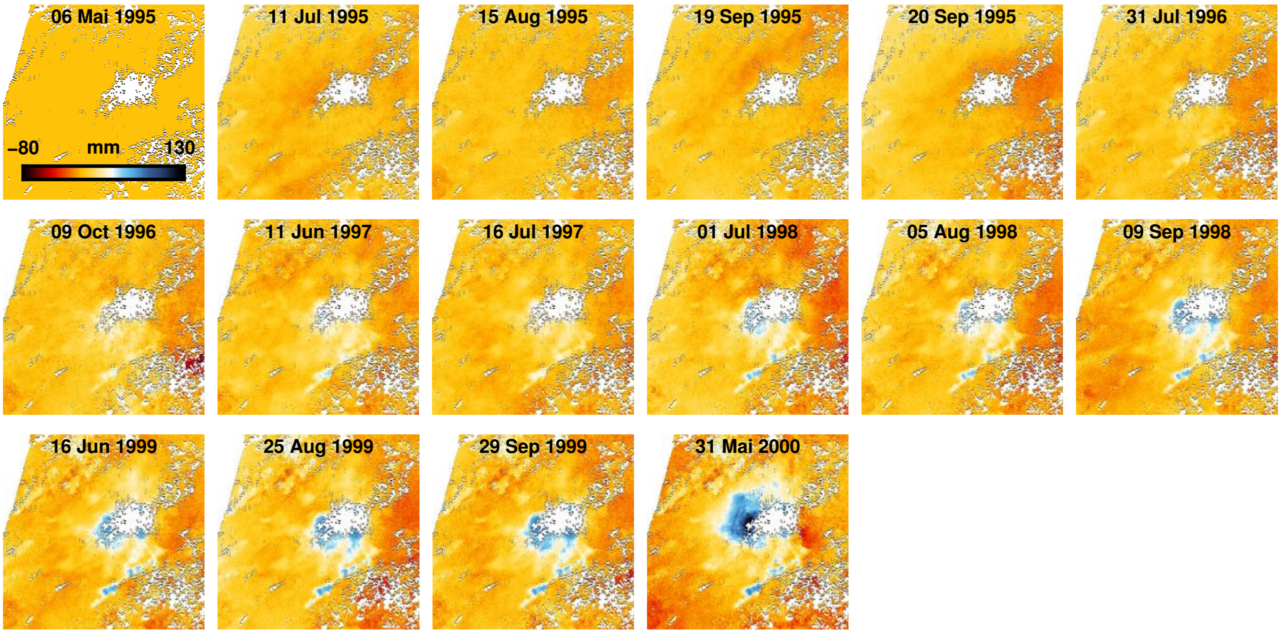

Figure S2. ERS time series spanning 1995 to 2000. Accumulated LOS unwrapped phase change, Track 324, descending.

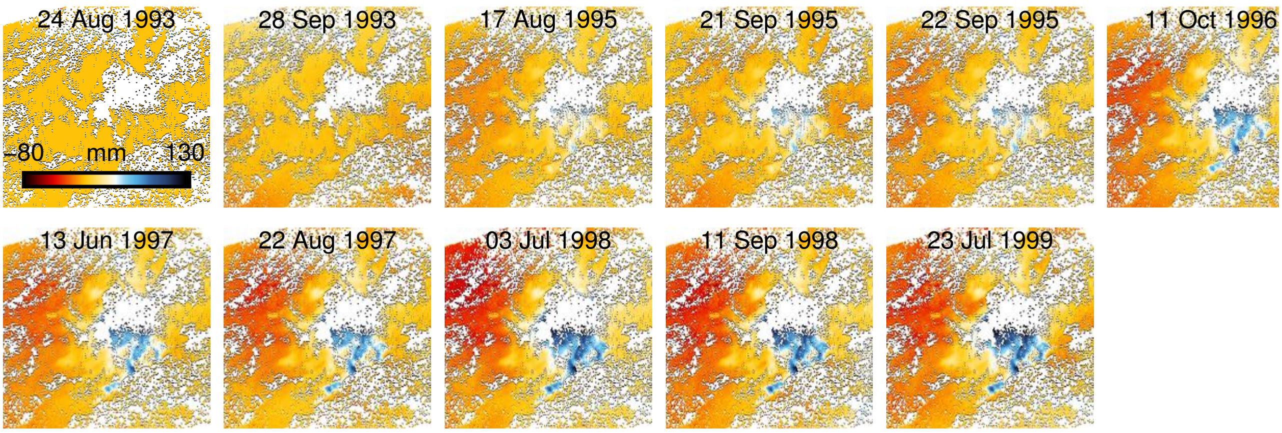

Figure S3. ERS time series spanning 1993 to 1999. Accumulated LOS unwrapped phase change, Track 359, ascending.

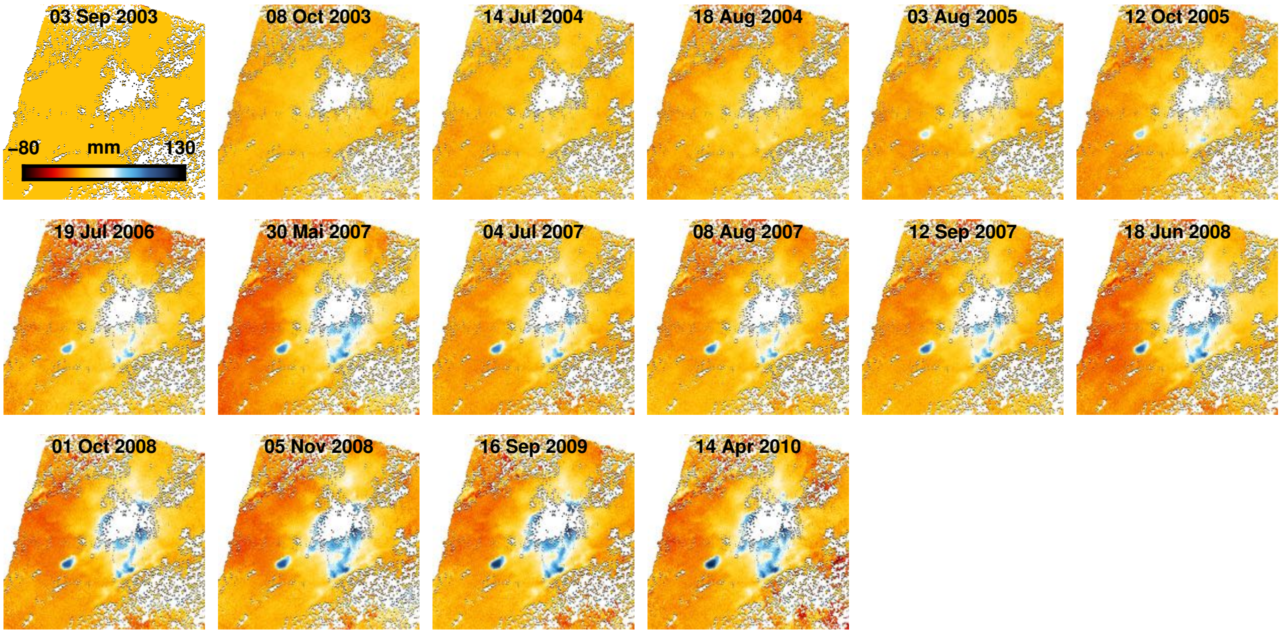

Figure S4. Envisat time series spanning 2003 to 2010. Accumulated LOS unwrapped phase change, Track 324, descending.

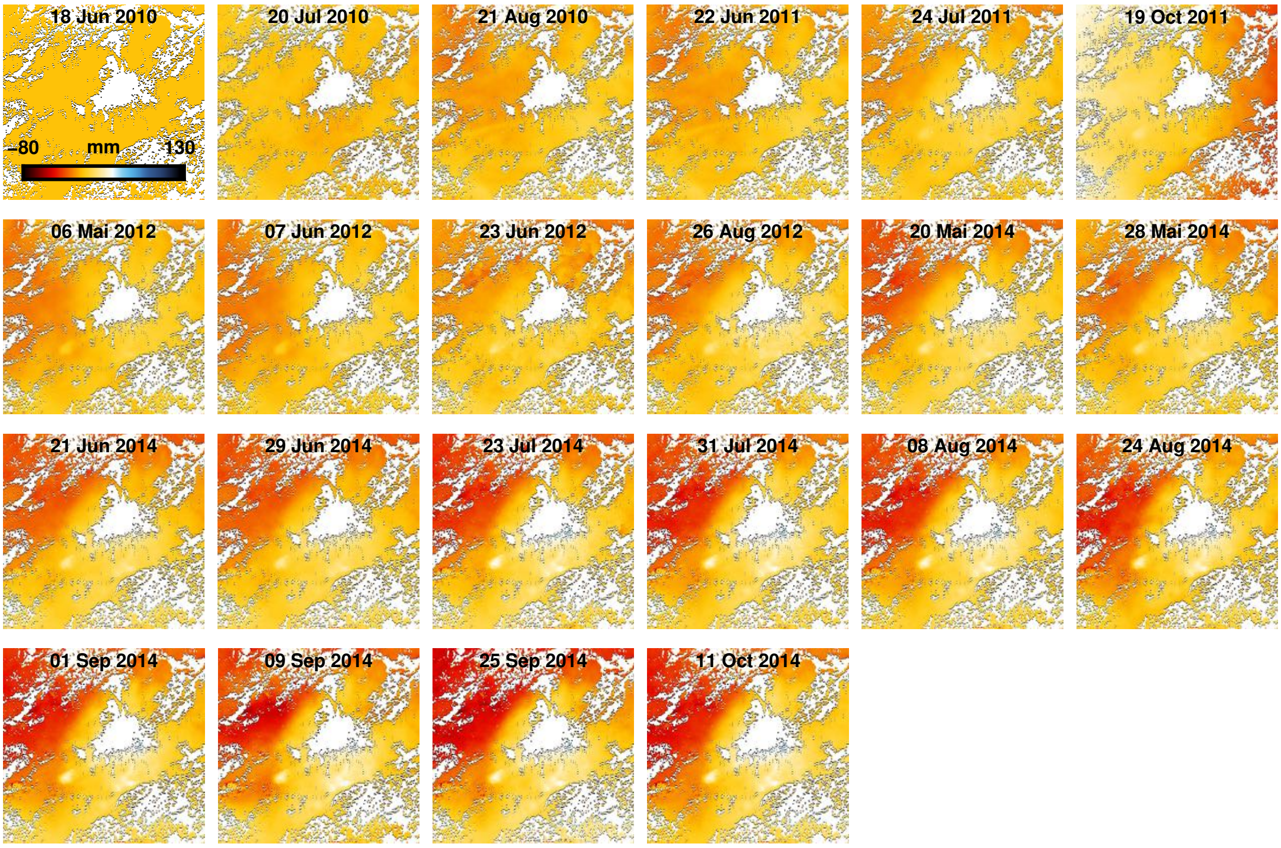

Figure S5. CSK time series spanning 2010 to 2014. Accumulated LOS unwrapped phase change, Track 2574, ascending.

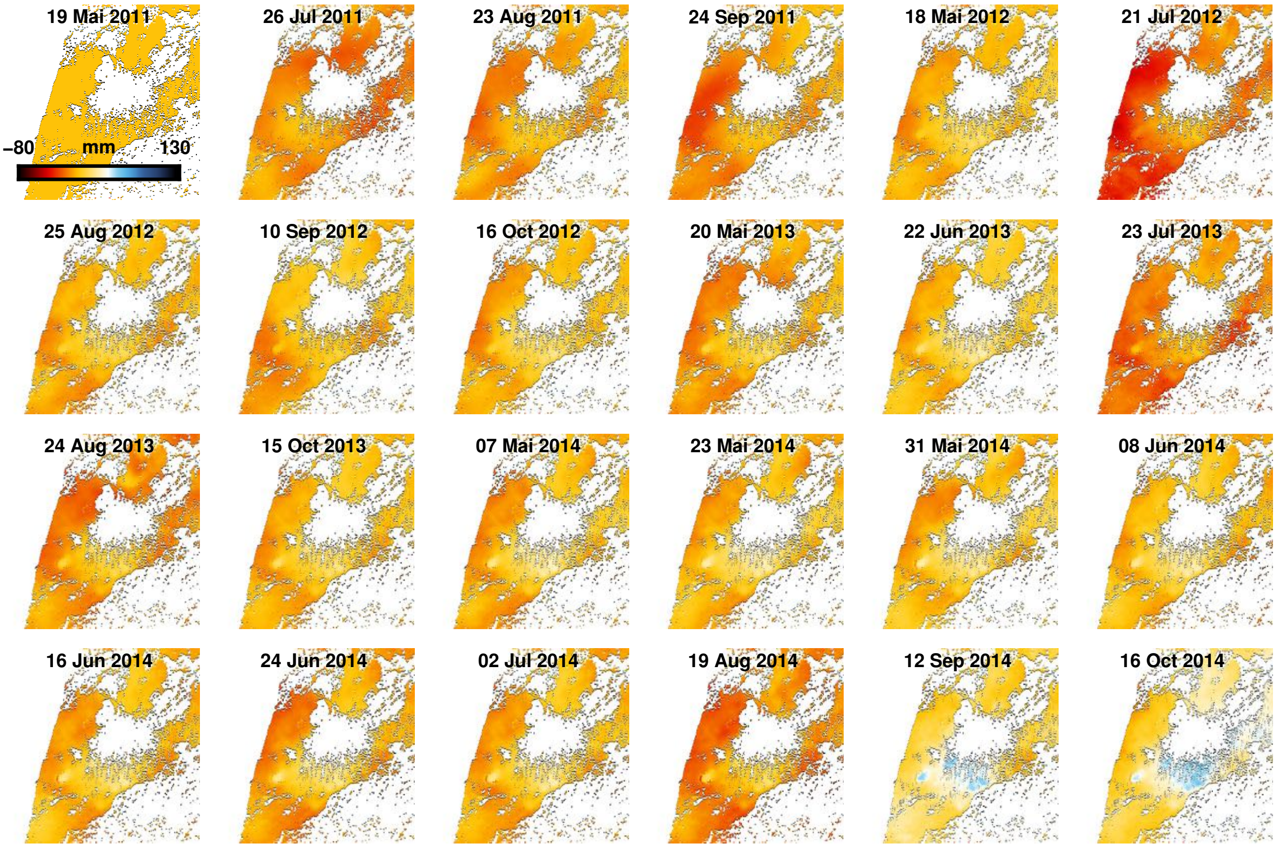

Figure S6. CSK time series spanning 2011 to 2014. Accumulated LOS unwrapped phase change, Track 2575, ascending.